CHAPTER 4

4 RESULTS AND DISCUSSION

The characterization findings for the copper-clad steel are discussed in this chapter. The obtained clad was first visually examined for any obvious flaws or flashes, and the samples that were defect-free were chosen for further characterization. This chapter describes the findings of metallography, X-ray radiography, and mechanical tests such as tensile, microhardness, and guided bend test results. This chapter also includes an examination of the corrosion test results for comparison of the performance of clad copper to base copper and base steel. The AFM analysis has also been carried out to evaluate the corroded surface and understand the corrosion mechanism.

4.1 Results for copper clad aluminium

As discussed earlier, in section 3.4.1, before attempting the cladding of copper on steel, copper on aluminium was performed. This section gives the metallography results for the cladding of copper on aluminium. The metallography of the copper-clad aluminium plate was carried out on the transverse cross section. The cross section of the samples, when observed at a magnification of 100X under an optical microscope, revealed good interfacial bonding between the clad material and the substrate, as shown in Figure 4-1. With each subsequent pass of FSW, the clad layer covered a greater width of the clad sample and showed good bonding between the clad copper and the aluminium substrate. The portion of the previous pass underwent another partially overlapping FSW pass, which resulted in more intense intermixing of the clad

and substrate material with an increasing number of passes, as shown in Figure 4-1b. Typically, long chunks of copper, having a length of greater than 250 microns, are fragmented from the parent copper and distributed near the interface. In such cases, the substrate material also moved greater distances (in the vertical direction) away from the interface due to repeated stirring. Small copper fragments were scattered over large distances, as seen in Figure 4-1c and Figure 4-1d. The SEM image depicting the interface region has been shown in Figure 4-1e illustrating good bonding between copper and aluminium substrates, while the magnified image of the same has been shown in Figure 4-1f. The clad layer on top consisted of pure copper with no dilution from the substrate material. Thus, initial attempts at cladding copper with aluminium gave successful results, and thereafter, trials for cladding copper with steel were initiated.

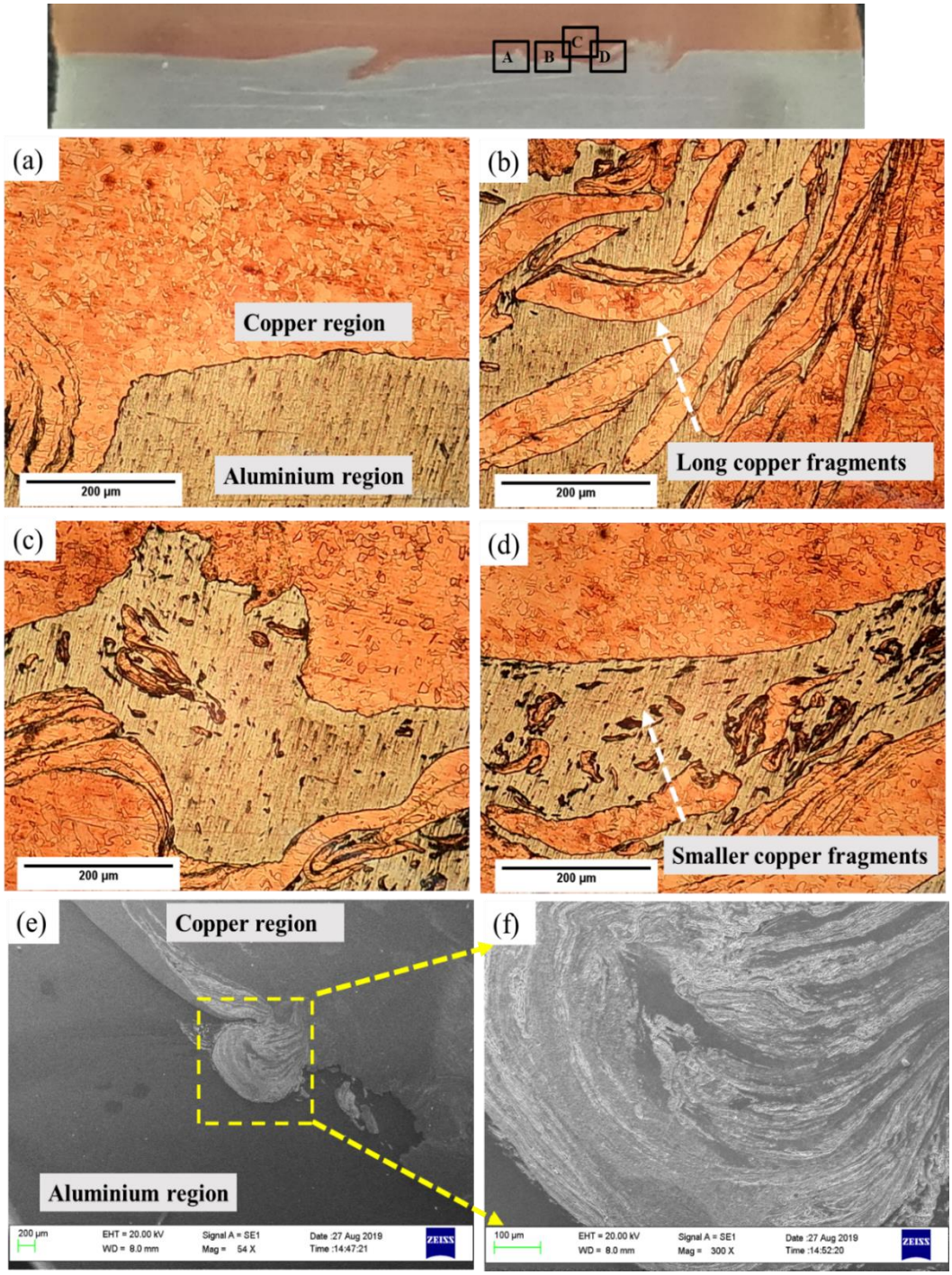

Figure 4-1 Optical microstructure of copper clad aluminium (a) showing interface (b) depicting long copper fragments near interface (c) & (d) indicating small copper chunks distribution (e) SEM image of interface (f) magnified image of same

4.2 Issues during cladding of copper on steel

After the successful demonstration of cladding copper on aluminium, attempts to clad copper on steel were initiated. Initial attempts faced numerous challenges. During

cladding, several issues need to be taken care of for a successful clad, which are generally not faced during welding in lap or butt positions. This section critically evaluates the various obstacles faced during the cladding of steel with copper. Cladding differs from normal butt welding as, over here, multiple identical passes are required to be executed, which faces challenges in the form of tool deterioration, plate warping, selection of process parameters, etc.

4.2.1 Optimization of pin length and tool plunge

With a short pin length, the pin tip is not able to reach up to the copper-steel interface, and as a result, the tool pin is not able to stir the material at the interface region, where bonding is required, thus not causing the cladded material to bond with the substrate material as shown in Figure 4-2a. A short pin length leads to the tool exit hole with all copper.

Shoulder plunge is another important parameter that needs to be correctly set for successful cladding. Too large a tool plunge leads to a larger portion of the tool shoulder in the substrate region, generating excessive heat resulting in tool damage and tool wear, along with severe flash formations as shown in Figure 4-2b. Hence, optimum pin length along with the correct shoulder plunge is required so that the pin bottom just pierces the top portion of the mild steel substrate, resulting in proper stirring at the interface region as shown in Figure 4-2c.

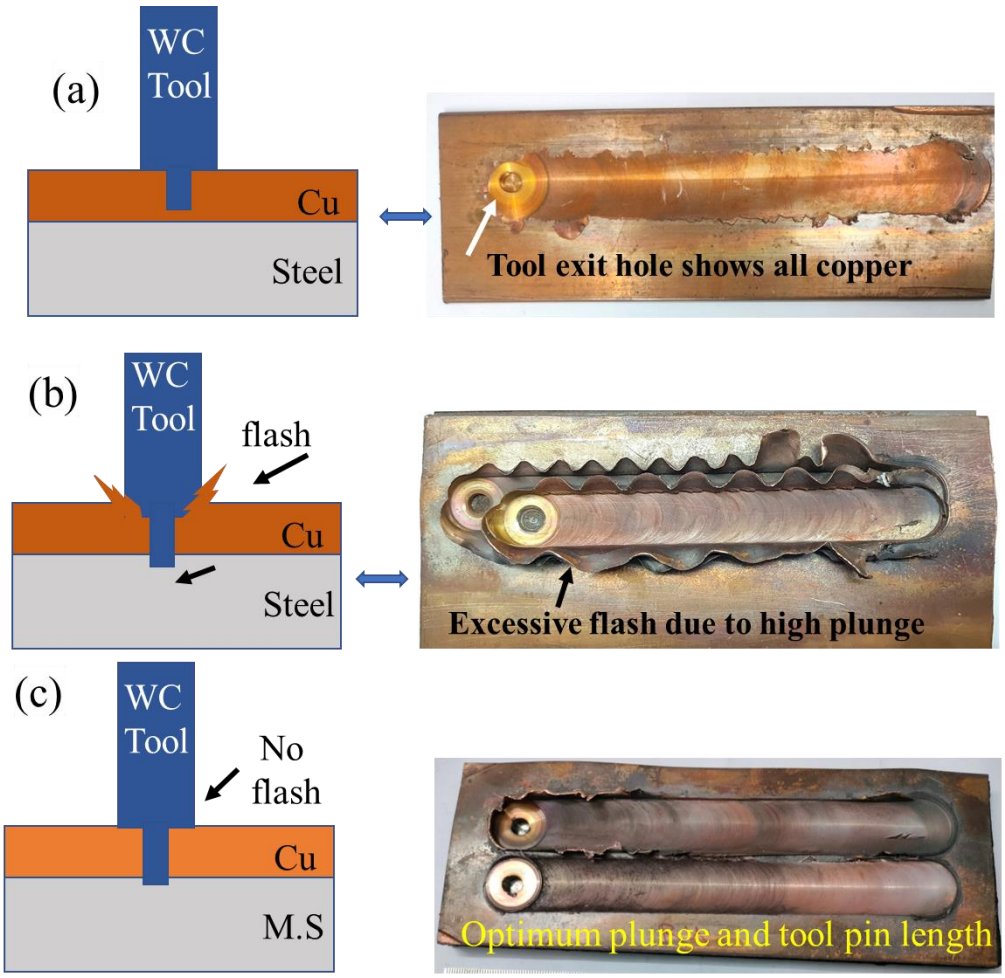

Figure 4-2 Illustration (a) for shorter pin length (b) for larger tool plunge generating excessive flash (c) optimum tool plunge and pin length

4.2.2 Cavity and defect formation during multi pass cladding

An important aspect of multi-pass cladding is having proper material distribution around the sides during cladding. In the absence of that, cavity formation or tunnel defect formation can take place, as shown in Figure 4-3. This type of defect may arise either due to a sudden change in process parameters for the subsequent pass or due to insufficient material available for distribution, resulting in a deficiency of material on the advancing side (as material distribution fills the advancing side in the last step).

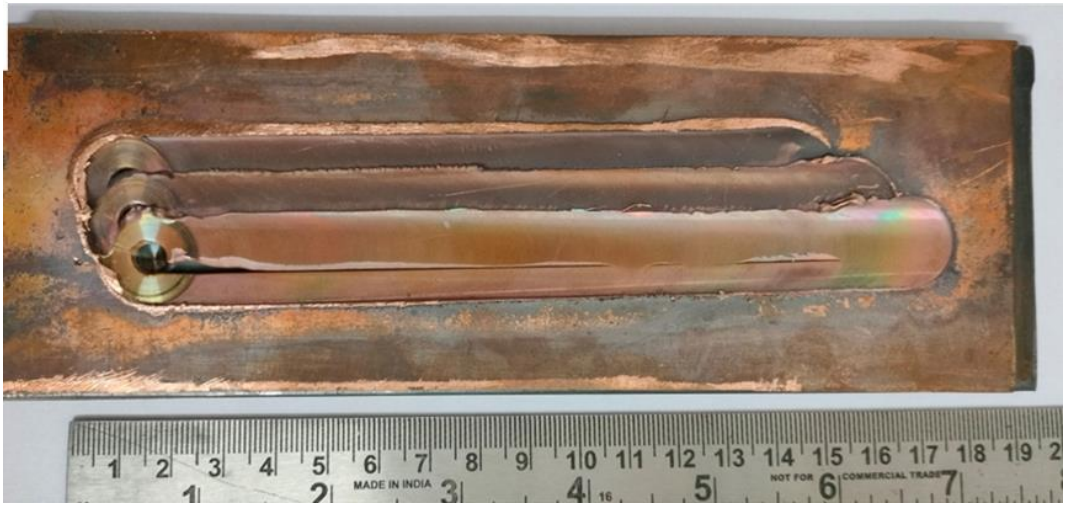

Figure 4-3 Cavity formation due to improper material distribution during multi pass cladding

4.2.3 Tool plunge for multiple passes

During multi-pass cladding, with each ongoing pass, the top surface of the clad material bulges out around the periphery of the tool, with a little more on the retreating side, as shown in Figure 4-4a. When the subsequent passes were made by keeping the tool offset distance corresponding to the shoulder radius, the pin fell directly on the top of the risen portion, providing an inaccurate tool plunge for the next pass, particularly because the FSW machine was run in position control mode in this work. Operating the FSW machine in force-controlled mode will take care of this issue to some extent. In this work, the subsequent passes were made by plunging the tool 10 mm further backwards in the y-direction, as shown in Figure 4-4c to take care of this issue.

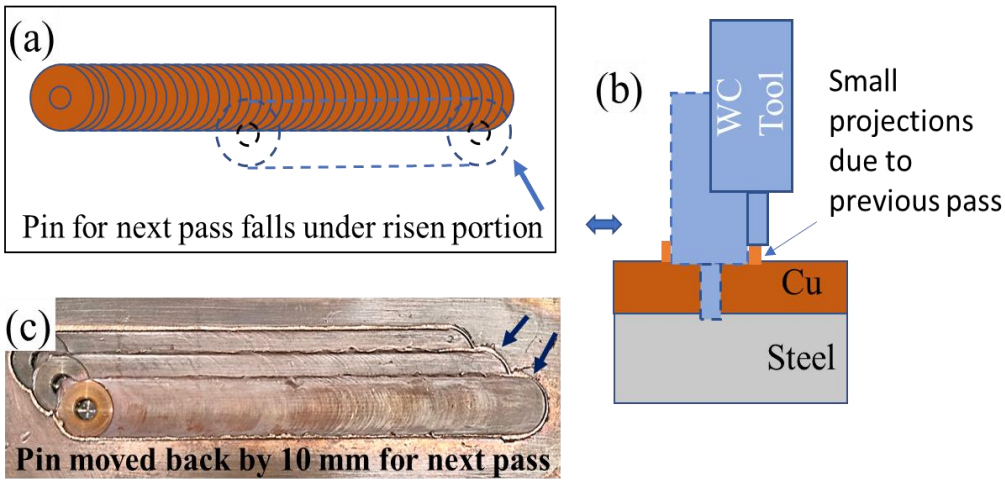

Figure 4-4 Schematic illustration for small projection arising during FSW creating obstacle for next pass and its preventive steps

4.3 Tool behaviour analysis

Tool degradation is one of the crucial aspects of FSW cladding, and in this work, maintaining the tool shape is one of the challenges. For cladding, in each pass we need to bring the tool tip up to the identical point, and if tool wear takes place, then for subsequent passes, the tool cannot move up to the same depth, i.e., an eroded tool skips several areas unbonded, resulting in a faulty clad layer.

In FSW, the rate of heat generation per unit weld length depends on the tool shoulder diameter, tool rotational speed, and welding speed. The rate of heat generation per unit length of weld increases with an increase in tool shoulder diameter and tool rotational speed for a certain welding speed. Thus, it is anticipated that a slower tool rotational speed and a faster welding speed will result in a lower rate of heat generation per unit weld length and a lower peak temperature.

Several kinds of pin damages were encountered in the tool pin of tool A and have been shown in Figure 4-5. Mushrooming of the pin has been shown in Figure 4-5a which also results in a depression in the height and an increase in the width of the pin [210].

Wear of the tool pin periphery has been shown in Figure 4-5b, while face wear of the pin has been shown in Figure 4-5c, which occurred due to the long cladding length travel of the tool pin. The tool also exhibited slightly black and bluish surfaces around the shoulder that can be attributed to oxidation during the plunging and dwell stages. Tool pin breakage in tool B is due to high forces and has been shown in Figure 4-5d. While in the case of cladding copper on aluminium, the tool did not encounter any deformation of the tool pin (mushrooming or pin periphery wear), rather it showed sticking of substrate material at the base side of the pin face, as shown in Figure 4-5e. The sticked material was required to chip off before carrying out the next pass, or else defective cladding was obtained due to the usage of an aluminium substrate sticked tool.

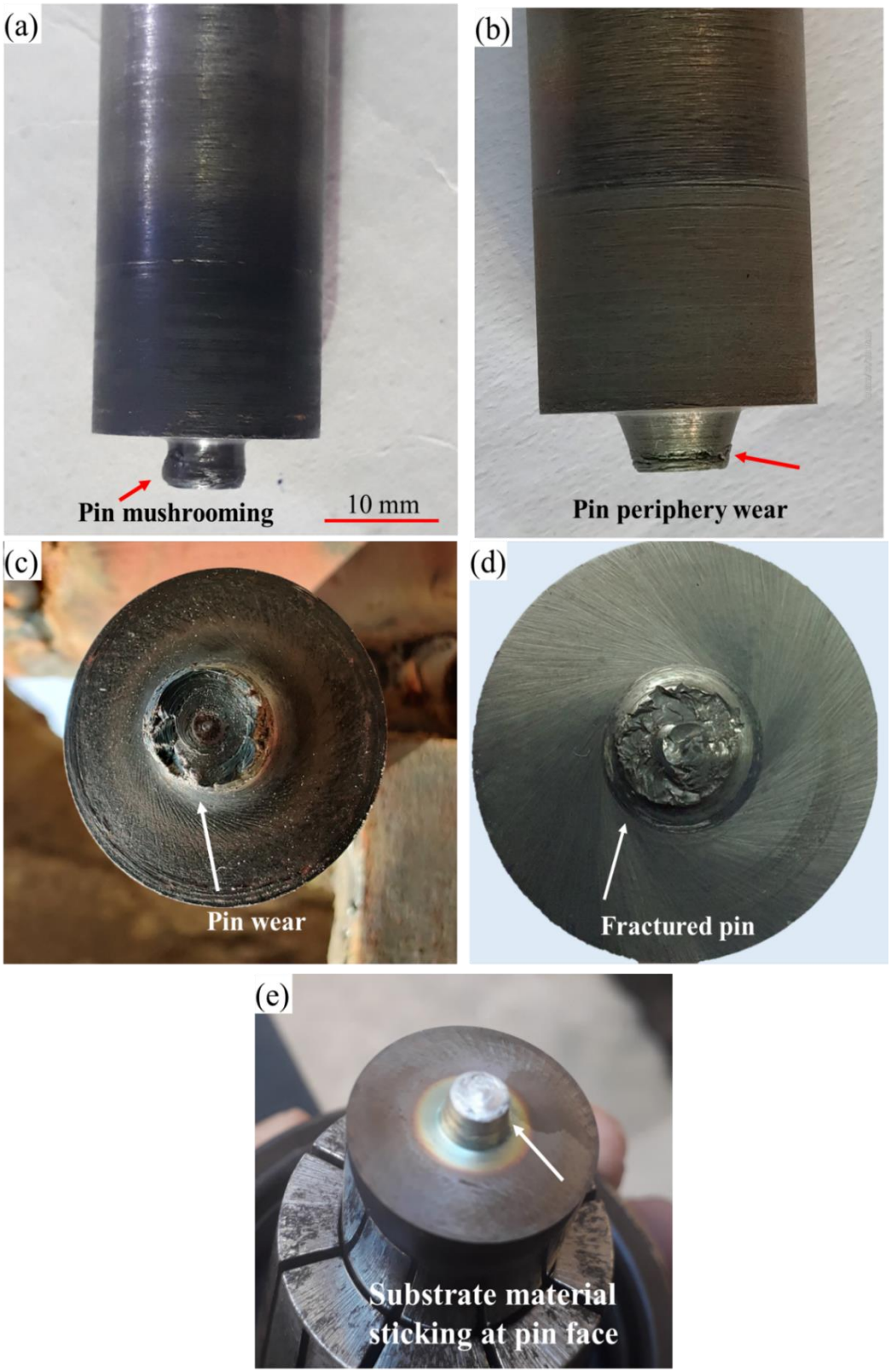

Figure 4-5 Tool defects during cladding copper on steel (a) pin mushrooming (b) pin periphery wear (c) pin face wear (d) tool B after pin breakage (e) aluminium substrate sticking on pin face for copper clad aluminium

Figure 4-6 demonstrates the SEM images of wear taking place in the face region of the tool, shoulder, and pin. Figure 4-6b is the magnified image of the tool pin shown in Figure 4-6a. Figure 4-6c shows the portion with crack generation marks and erosion of the pin due to abrasion. While Figure 4-6d shows the magnified image of the cavity produced in the tool pin due to abrasion, resulting in particle dislodgement from the pin face. Figure 4-6e shows the appearance of radial grooves in the shoulder region due to abrasion, while Figure 4-6f depicts the SEM image of the pin region, where the sticking of a thin work material layer can be seen, which occurs due to adhesion between the pin face and work material. Heavy wear of tool material A is due to the presence of a high amount of (cobalt + nickel >10%) as binder material. Choi et al. reported that at high temperatures, higher binder percent escalates the degradation of the binder cobalt phase, thus promoting abrasion wear resulting in particle dislodgement. The authors added that during tool exposure to high temperatures and forces, the tool undergoes plastic deformation, involving dislocation movement and twin formation, which results in the transformation of the face-centred-cubic (FCC) structure Co binder into the more brittle, hexagonal close-packed structure (HCP) Co, which subsequently alters the mechanical characteristics of the WC. The author also added that WC exposed to cycling fatigue exhibits reduced fracture toughness, erosion resistance and thermal shock resistance [211].

Similar results were reported by Tiwari et al., where degradation of WC-6%Co and WC-10%Co tools was reported during the FSW of DH36 steel, and the fracture of the tools was attributed to the transformation of the Co binder from the FCC to the HCP structure at high temperature [212]. The performance of low-cobalt nickel-bonded WC tools has been evaluated and discussed by Vicharapu et al., and the authors added that although tools' fracture toughness increased with the addition of nickel as a binder in

comparison to tungsten carbide tools, rapid tool degradation was observed [213]. According to the authors, two different wear mechanisms were responsible for tool degradation. Adhesion caused a worn-out shoulder surface, while abrasion caused the appearance of radial grooves on the probe surface. The author also added that with an increase in weld length, the tool suffered material loss. Overall, at greater tool rotating speeds and slower welding speeds, the tool's damage from oxidation and wear remained substantial. The wettability and adhesion of the tungsten carbide are greatly improved by the addition of cobalt, along with its strength and toughness. However, the hardness and wear resistance are inversely correlated with the cobalt content [214]. Thus, it could be concluded that for the cladding of copper on steel, a tungsten carbide tool with a low cobalt percent and typically a smaller grain size (2–4 microns) works well.

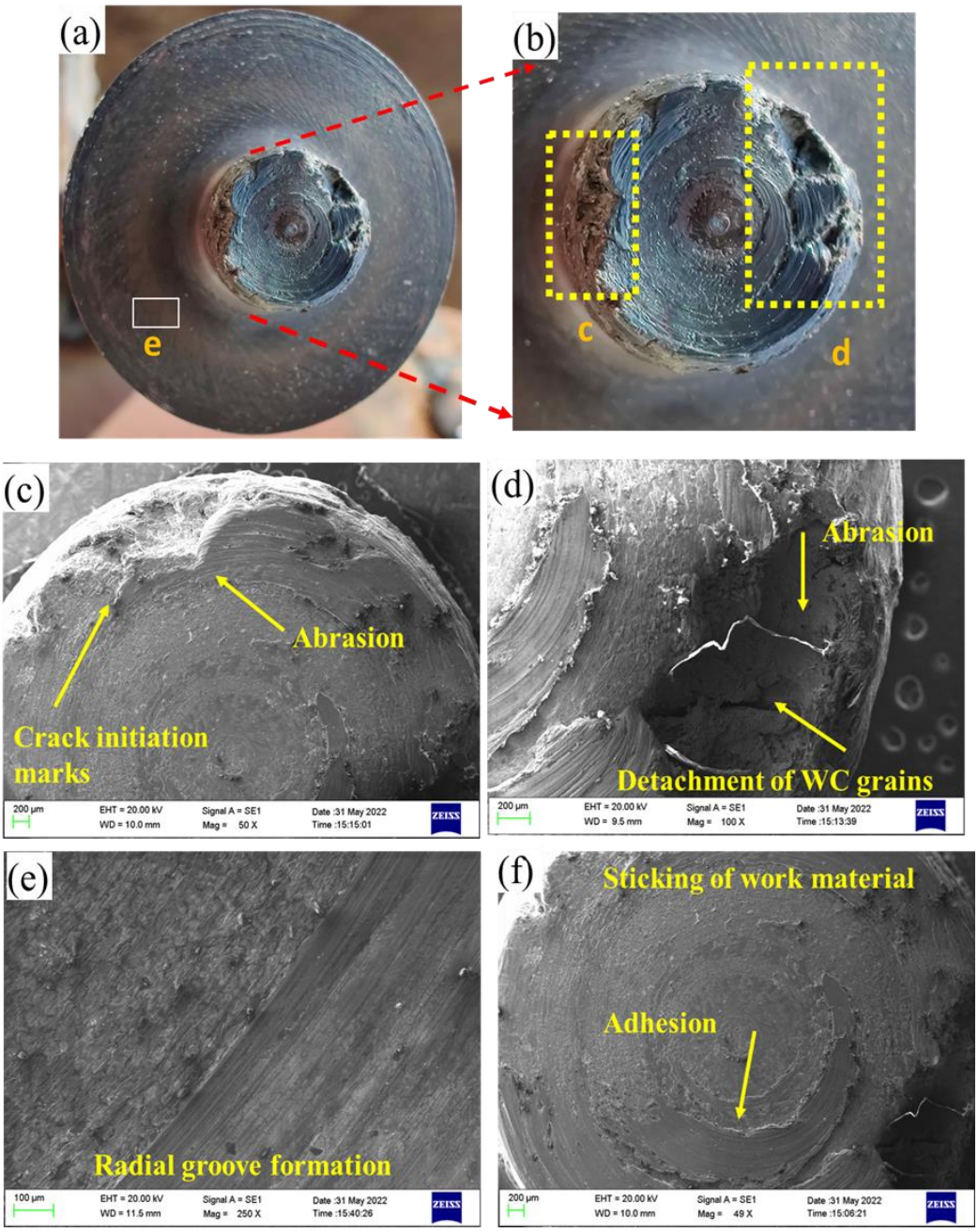

Figure 4-6 SEM image of face wear of 'tool A' pin depicting (a) entire tool face with shoulder (b) enlarged pin face (c) pin periphery demonstrating crack initiation and abrasion (d) material uprooting and cavity formation (e) radial groove formation in shoulder (f) sticking of work material in pin due to adhesion

SEM mapping of the tool pin has been shown in Figure 4-7, indicating the distribution of various elements obtained in the EDS analysis. The appearance of iron and oxygen in the EDS analysis shows the influence of adhesion with work material and oxidation wear, respectively.

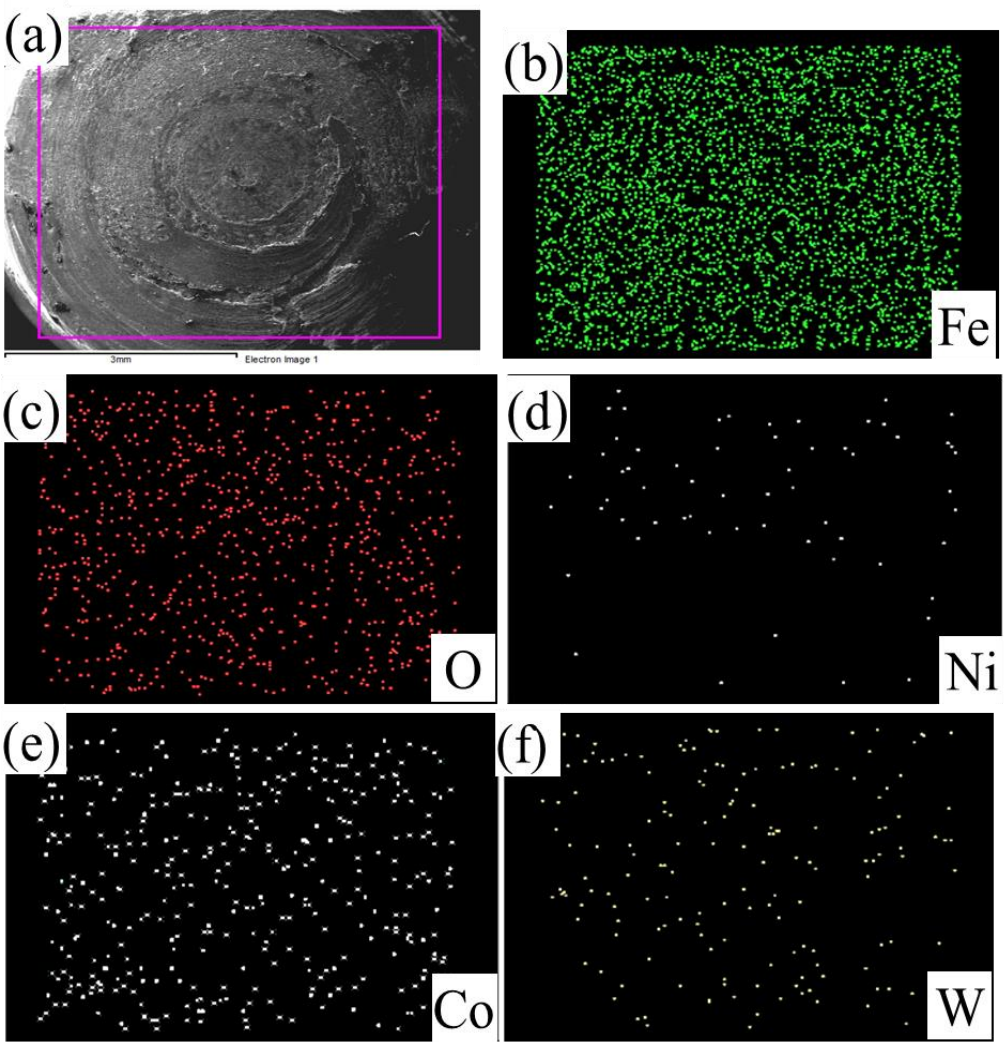

Figure 4-7 EDS mapping of 'tool A' pin surface

4.4 Results for copper clad steel with 3 mm minimal offset

After a successful demonstration of cladding copper on aluminium, attempts were made to clad copper on steel. FSW-cladded samples were prepared for single pass, double pass and triple pass as shown in Figure 4-8. An offset distance equal to the radius of the tool pin was given for double and triple passes. The intention over here was to first clad the samples effectively and observe the obtained results. The schematic diagram shown in Figure 4-9 shows how the offset can be determined so that no portion of the plate being cladded remains un-joined to the substrate. It is well

known that the plastic flow of steel during the copper cladding of steel is limited. Therefore, the initial offset chosen in this study was kept equal to the radius of the tool pin, i.e., 3 mm. This value was chosen in line with the values chosen by other researchers working on multi-pass lap welding.

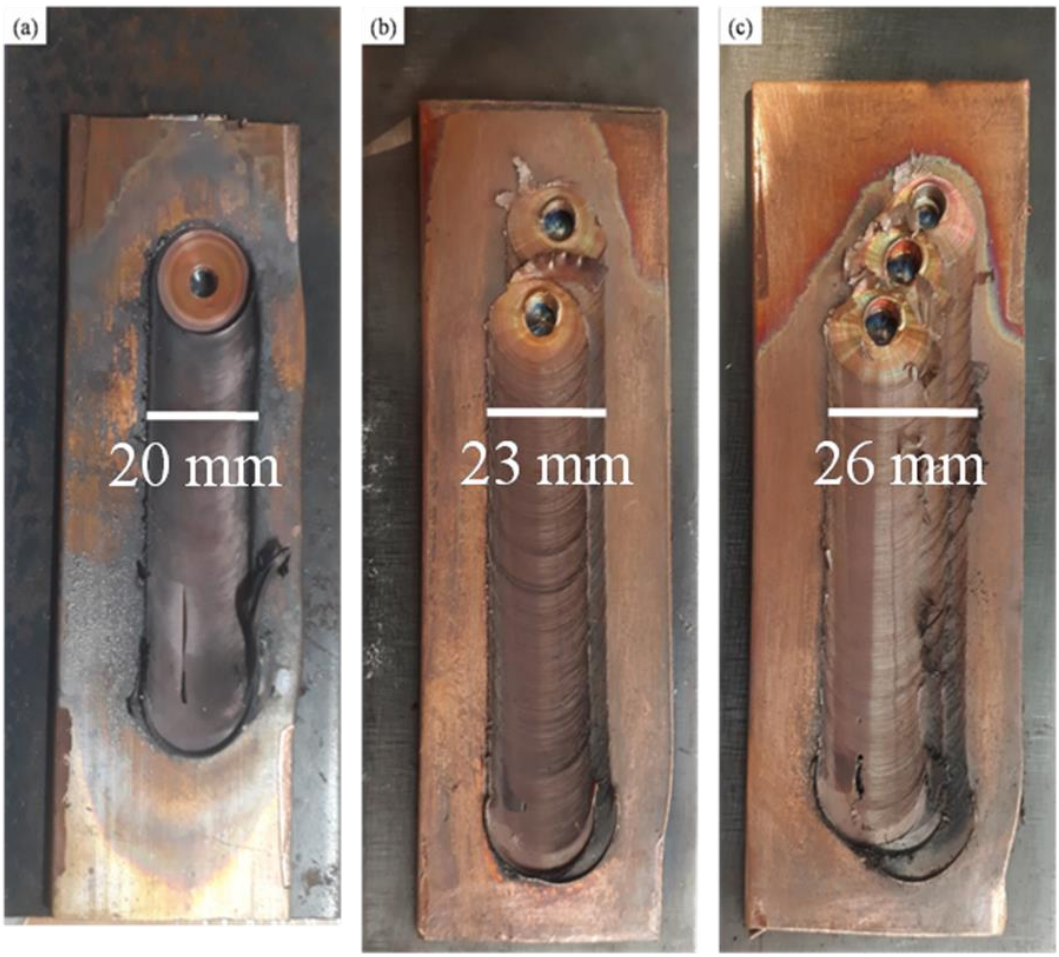

Figure 4-8 Photograph of cladded samples for different passes (a) one pass (b) two pass (c) three pass

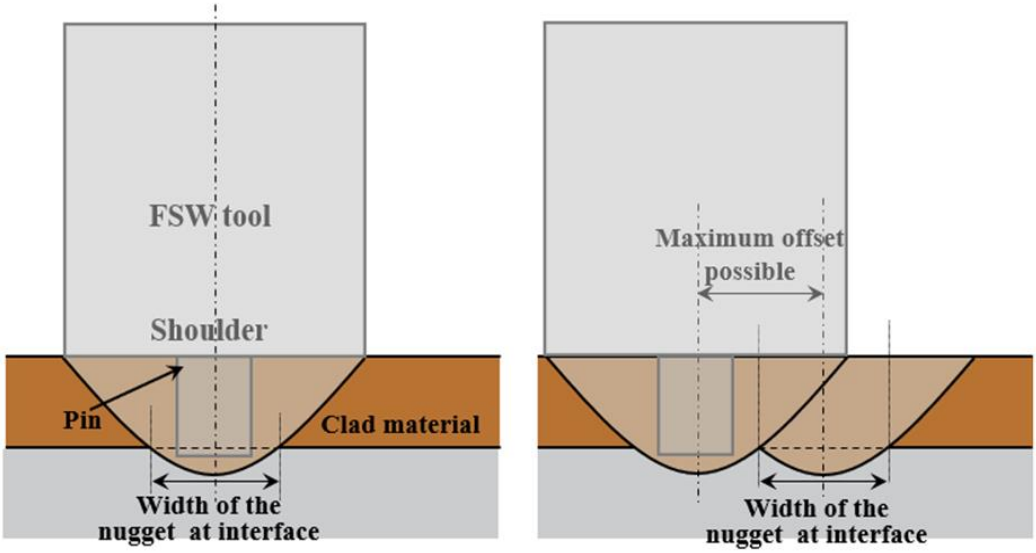

Figure 4-9 Schematic diagram showing the extent of overlap at the clad-substrate interface during any two successive FSW passes

4.4.1 Visual inspection of cladded plates

Visual inspection of Cu-clad steel samples, as shown in Figure 4-8, revealed defect-free cladding and a good bonding appearance. The region below the shoulder is clearly visible, comprising substrate material and very little flash was generated along the periphery of the clad region. For the single-pass cladded sample, a shoulder void defect was observed near the point where the tool was plunged and continued for around 20 mm before getting removed as the tool further traversed in the forward direction. These defects were restricted to the point of plunge in subsequent cladding passes. This defect is possibly due to the flowability difference between steel and copper during the initial stages, which later merges out. Samples exposing the transverse cross section of the clad portion have been shown in Figure 4-10. Multiple nugget centres can be clearly seen for a triple pass, while a single nugget centre is present in a single pass clad sample.

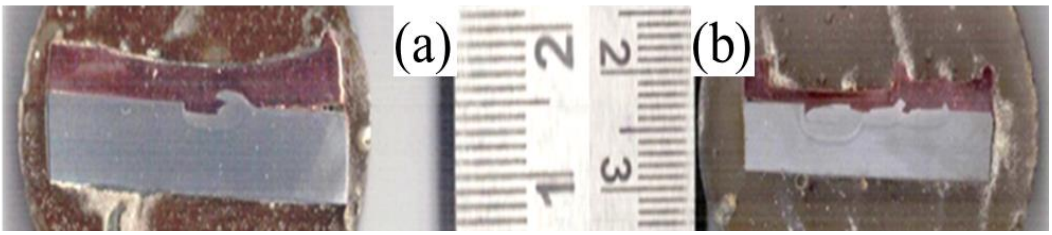

Figure 4-10 Transverse cross section of cladded sample for (a) single pass (b) multipass

4.4.2 Temperature variation during cladding operation

As described in section 3.5.2, temperature variation was recorded through a non-contact FLIR (forward-looking infrared) camera. Figure 4-11 shows the temperature variation during tool plunge, tool traverse and tool withdrawal, with images taken at an interval of 10 seconds. Figure 4-11a represents the photograph of the arrangement of plates for cladding, on which later images have been captured through the FLIR camera. During FSW, the temperature rise takes place in stages. Initially, the lower portion of the tool pin touches the clad surface, giving it a sluggish rise in temperature. This step is followed by a gradual plunge of the tool pin, where the temperature rises quickly, as shown in Figure 4-11(b, c, and d). The tool shoulder comes into contact at last, causing a rapid increase in total heat generation and a sudden increase in temperature. This can be observed clearly in Figure 4-11(e and f) where a temperature surge took place from 466 degrees Celsius to 630 degrees Celsius, within a span of 10 seconds. An initial dwell period of 10 seconds was provided to soften the surroundings for easy traverse of the tool in the forward direction. Temperature rise was also observed during the dwell time, as can be seen in Figure 4-11g, where the temperature rose above 660 degrees Celsius, and thereafter remained elevated throughout the cladding operation. Figure 4-11i represents the image after tool withdrawal, showing a drop in temperature after tool withdrawal.

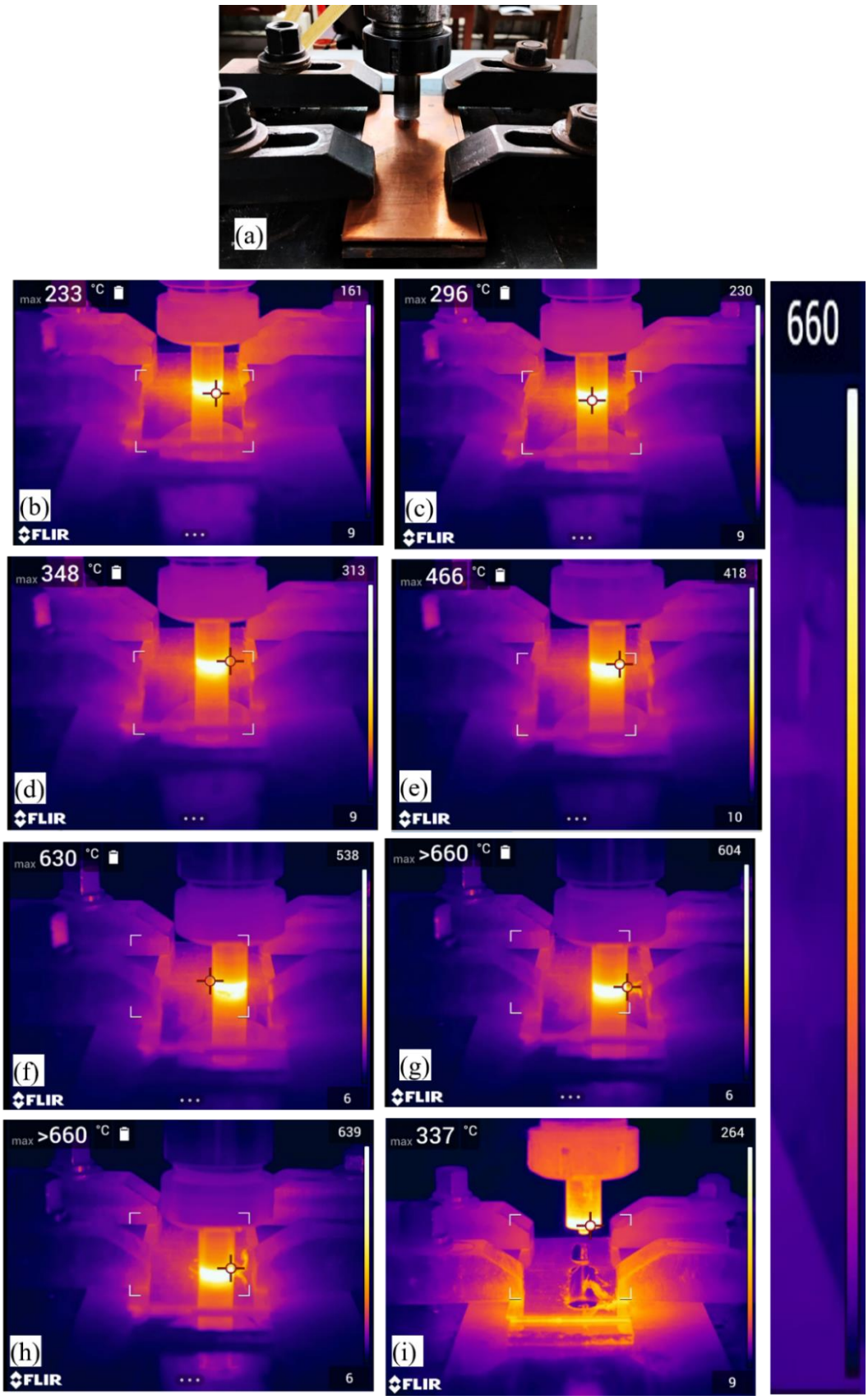

Figure 4-11 FLIR images indicating temperature variation during tool plunge and tool traverse

A pictorial graph has been shown in Figure 4-12 with temperature rise across the several stages, with highest temperature for cladding operation assumed at 800-degree Celsius (below the melting point of copper as the used FLIR camera could only measure up to 660-degree Celsius).

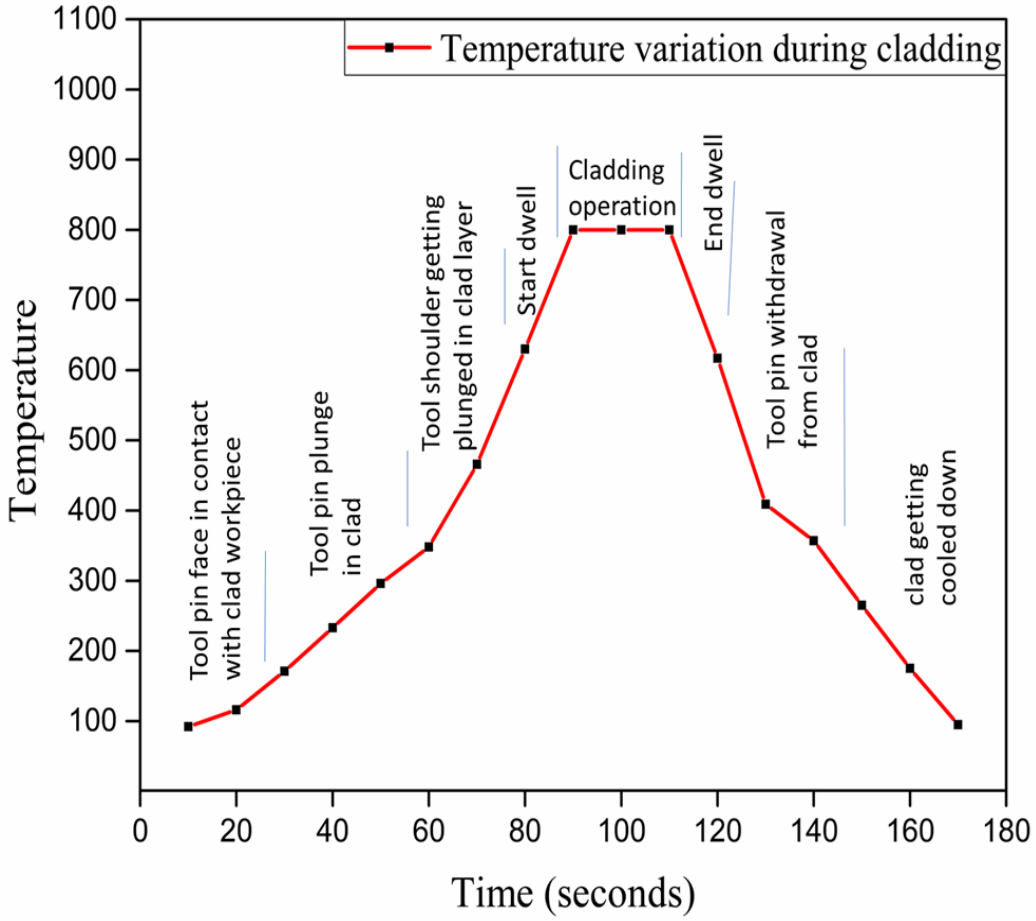

Figure 4-12 Temperature variation at different stages during cladding

4.5 Metallography of copper cladded steel

Metallography proves to be a crucial characterization technique to evaluate the microstructure and bonding quality of the prepared specimens. Various images have been captured and compared through optical and scanning electron microscopy. SEM mapping has been utilised to reveal the elemental distribution across the boundary.

4.5.1 Optical microstructure evaluation

Optical micrographs of single-pass and multi-pass (three-pass) copper-cladded steel are shown in Figure 4-13 and Figure 4-14 respectively. The macrostructure of the transverse cross section of the clad area is displayed at the top, with various sites indicated with a, b, c, d, and e, and has been shown to indicate the locations from which micrographs have been captured.

The microstructure of the received steel has been shown in Figure 4-13a and can be seen to consist of a typical ferrite pearlite microstructure with an average grain size of 10.9 µm. Figure 4-13b shows the microstructure of the nugget zone where copper has mushroomed and penetrated into the mild steel substrate, demonstrating strong mechanical interlocking between the substrate and clad material. Adjacent to this site, in Figure 4-13c surface jetting profile was observed near the interface, resembling the feature that is typically seen in explosively welded samples. This wave-type appearance occurs due to Kelvin Helmholtz instability produced across the interface, near the pin travel region. This instability occurs when there is velocity shear at the interface between two layers of materials with different densities. This wavy interface could be produced on the entire surface by multiple FSW passes (tool travel) in the entire clad region with a minimum tool offset. Also, due to intense stirring in the nugget zone, dynamic recrystallization took place, resulting in grain refinement in the nugget area, as shown in Figure 4-13b and Figure 4-13c with the average grain size reducing to 3.9 µm from the initial 10.9 µm. A continuous oxide layer interface was also observed in the shoulder region in Figure 4-13d, and the region was not accompanied by grain refinement and had an average grain size of 8.89 µm. The interface below the

shoulder on the other side of the pin was not continuous, and the bonding was also not proper, as it can be seen in Figure 4-13e.

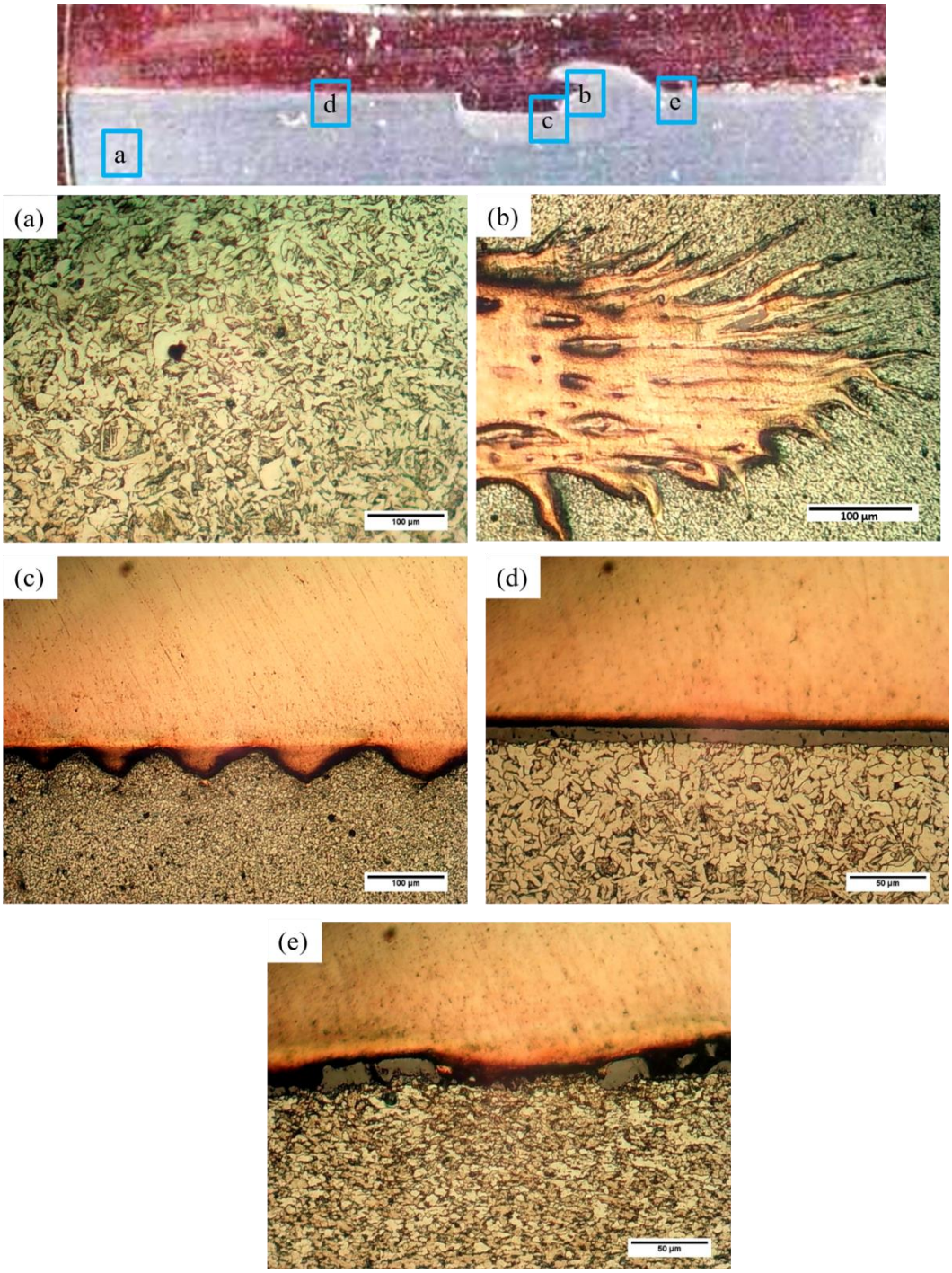

Figure 4-13 Optical microstructure of transverse cross-section of single pass copper clad steel at various indicated locations

For multi-pass cladding with three passes, similar observations were noted for steel substrates, such as grain refinement in the weld nugget zone as in Figure 4-14(a, b), with an average grain size of 4.2 μm, peak type formation as in Figure 4-14a, coupled with a continuous interface at the shoulder area as in Figure 4-14c. Along with these, some wavy type of microstructure is visible near the nugget area in Figure 4-14b of multipass pass cladding, suggesting better bonding of copper to steel with an increasing number of passes. Another noticeable observation was the flow of cladding material to distinct locations, as seen in Figure 4-14d, where copper exhibits much more flow of material than what was seen for a single pass of cladding. Figure 4-14e shows the portion where the steel region is shown encircled within the copper region.

With respect to single-pass, enhanced stirring and flow of clad copper material took place for multi-pass cladding, and it can be concluded that with an increasing number of passes, better and more uniform bonding is possible between clad and substrate material.

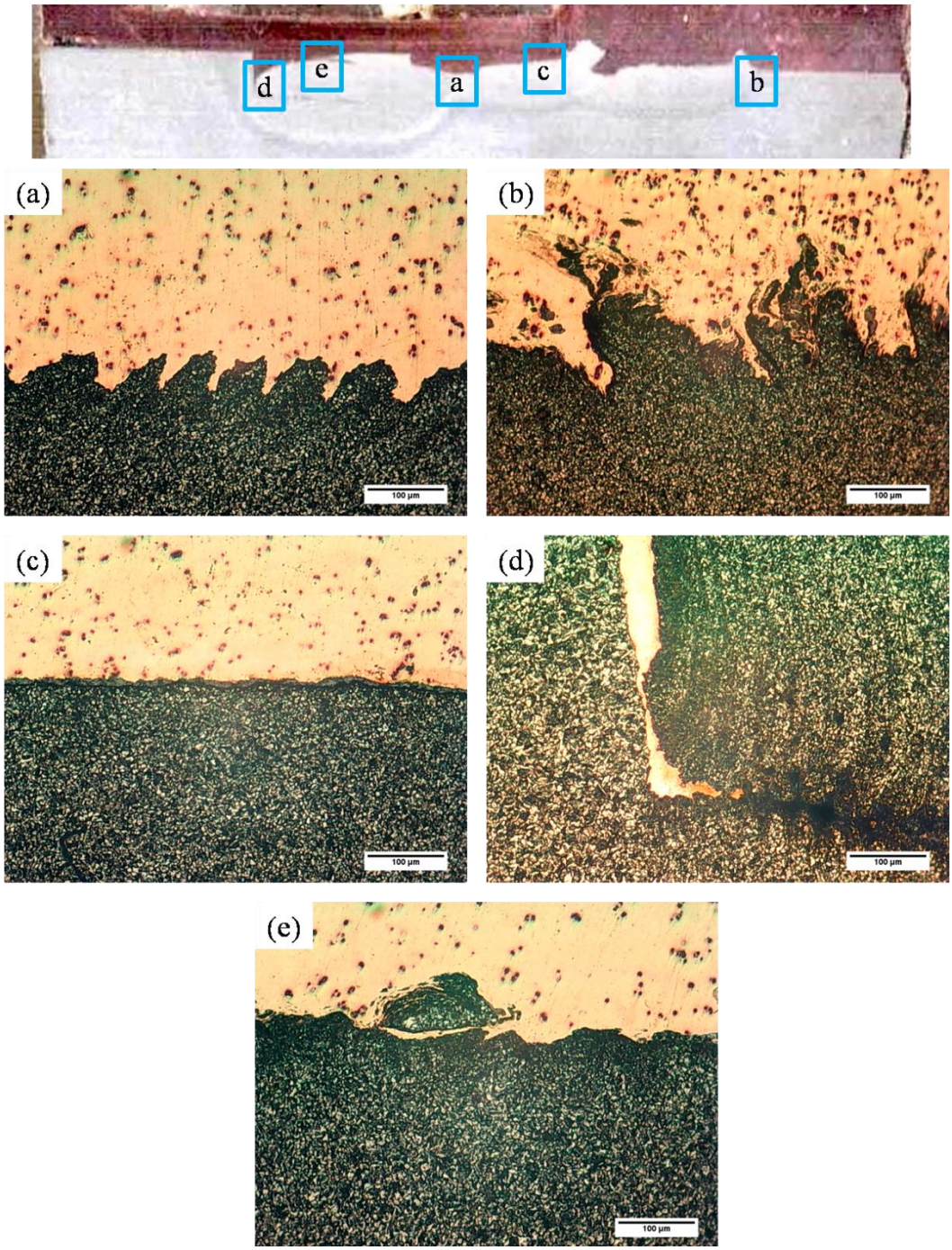

Figure 4-14 Optical microstructure of transverse cross-section of multi pass copper clad steel at various indicated locations

The average grain size variation across the steel substrate for different positions, i.e., base metal, nugget zone, and HAZ for single pass and multi pass, has been shown in Figure 4-15. The average grain size was measured using the intercept method, as shown by the inset in Figure 4-15. Nearly similar results, having a grain size of 4

microns, were observed near the nugget zone of single pass and multi pass due to grain refinement. The HAZ had a grain size of 5.3 microns during multi-pass cladding, which is smaller than the average grain size of 8.8 microns obtained in single-pass. The observation of more refined grains along HAZ of multi-pass clad steel is due to repeated stirring, resulting in smaller grains with an increasing number of passes.

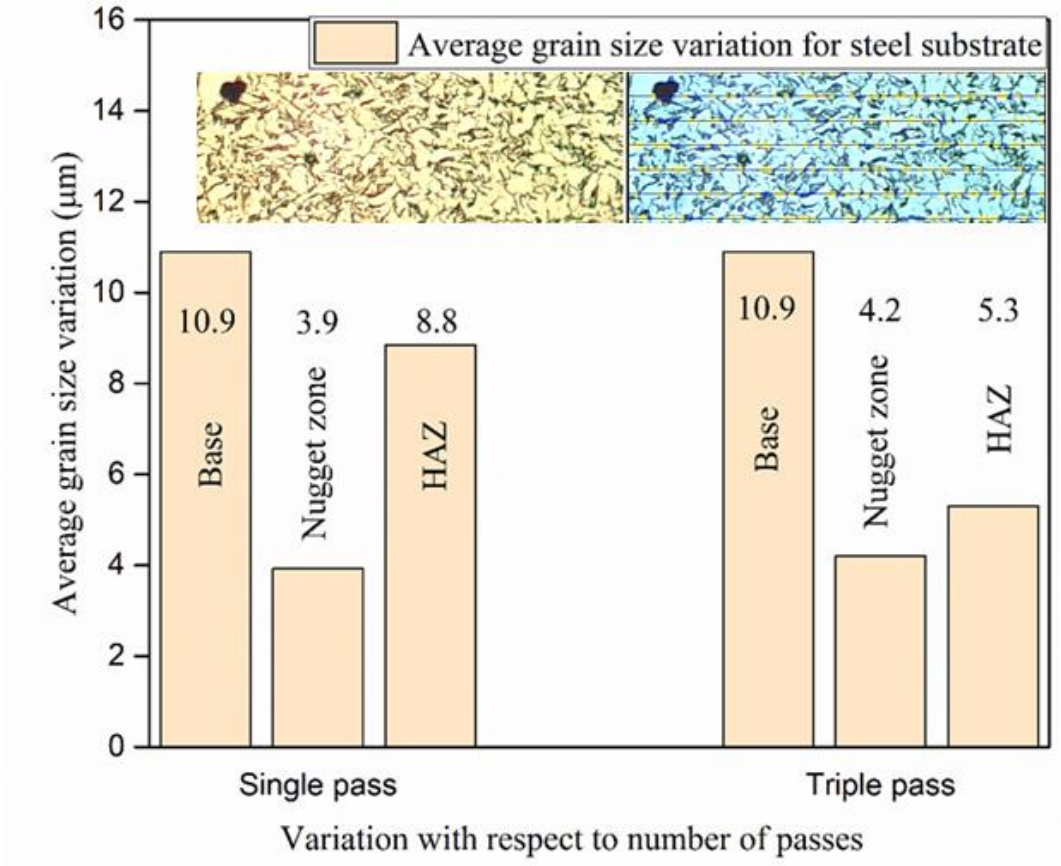

Figure 4-15 Grain size variation across different locations of steel substrate for single pass and multipass cladding

4.5.2 SEM, EDS mapping and its quantification

4.5.2.1 Copper clad steel single pass

SEM images of copper-clad steel after a single pass of the cladding at higher magnification revealed good bonding between steel and copper. Two microscopic defects (approximately 200 microns and 50 microns in size) missed out during optical

microscopy were observed under SEM and can be seen in Figure 4-16a and Figure 4-16b respectively. These defects were observed in two regions where gross plastic deformation of steel into copper has taken place, and the defects occurred due to the low plasticity of steel in comparison to copper. Such microscopic defects were not observed in regions where the gross plastic flow of copper into steel has taken place. However, it should be noted here that these microscopic defects were completely eliminated in multipass samples. Clear bonding was visible elsewhere on the cross section, even at a higher magnification of 1000X, as shown in Figure 4-16c. Near the top surface of the clad samples, the microstructure of copper was observed and has been shown in Figure 4-16d.

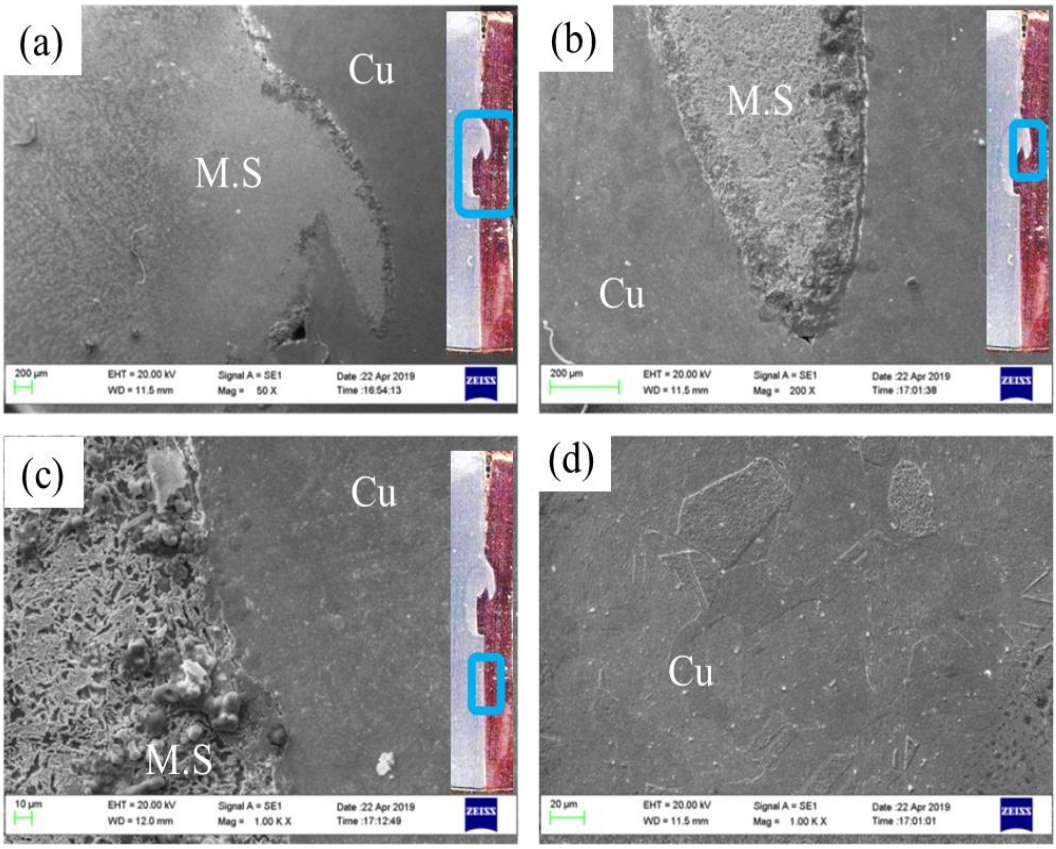

Figure 4-16 SEM micrograph of copper clad steel after single pass (a), (b), (c) are at different locations of transverse section (d) top face of clad layer

4.5.2.2 Copper clad steel three pass

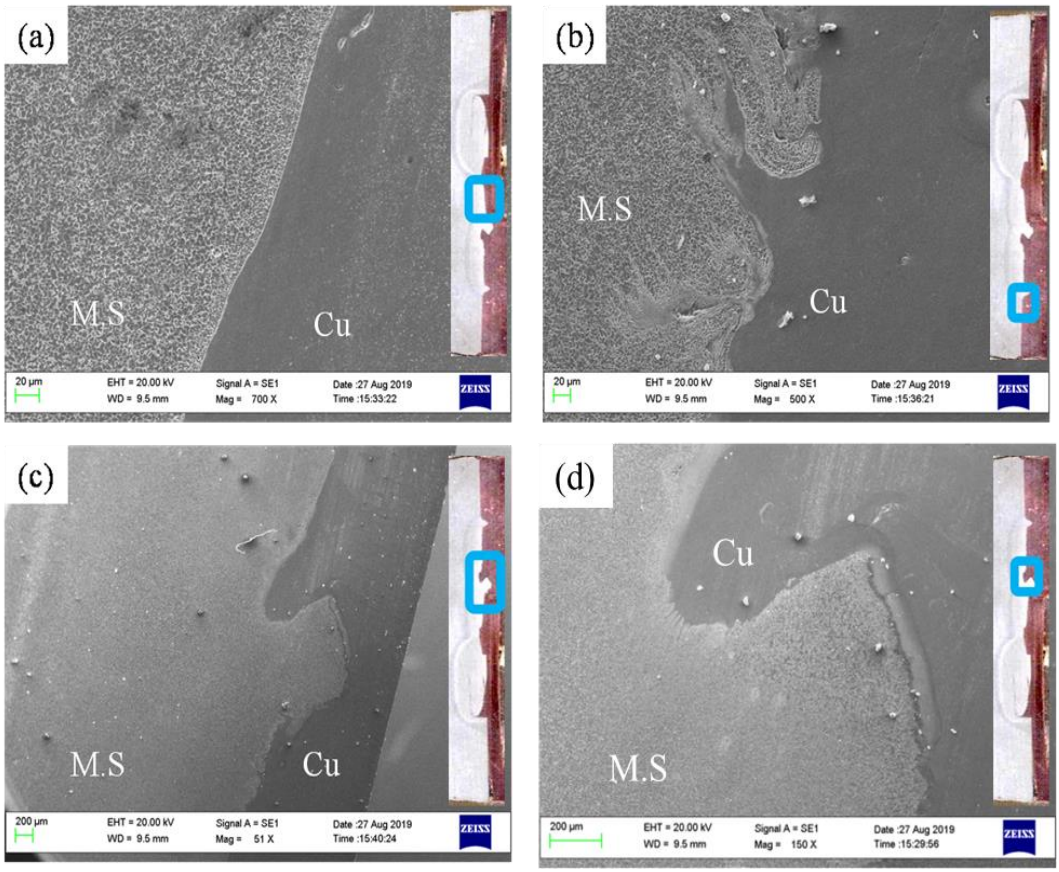

Figure 4-17 SEM micrograph of copper clad steel for three passes at various indicated locations

Figure 4-17 represents the SEM images for multi-pass copper-clad steel at different magnifications, where a properly bonded continuous interface was seen as in Figure 4-17a, while intense mixing is predominantly seen near the nugget zone as shown in Figure 4-17b, which was also observed during optical microscopy in Figure 4-14b. The mixing was also more uniform for multi passes. SEM observation at alternate locations of the sample revealed some uprooting and penetration of chunks of copper inside the mild steel, as shown in Figure 4-17c and Figure 4-17d respectively.

(a)

Element	Weight %	Atomic %
Fe k	64.28	67.18
Cu k	35.72	32.82

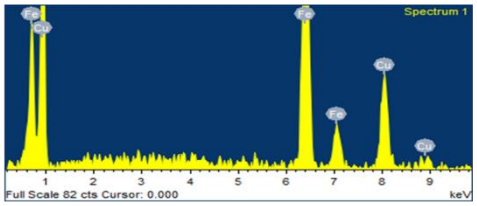

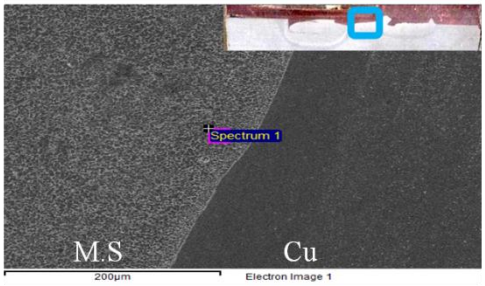

(b)

Element	Weight %	Atomic %
Fe k	42.19	45.36
Cu k	57.81	54.64

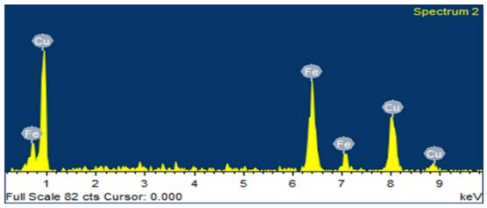

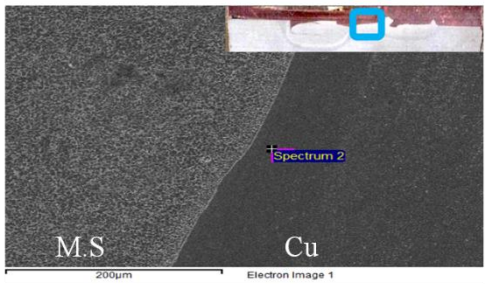

(c)

Element	Weight %	Atomic %
Fe k	49.77	52.99
Cu k	50.23	47.01

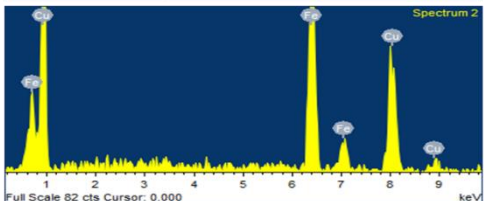

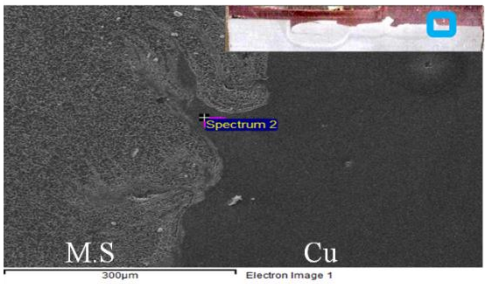

Figure 4-18 EDS quantification of different locations of three pass copper clad steel

Elemental analysis was carried out on both sides of the interface, on the transverse cross section, as shown in Figure 4-18. The three-pass clad samples revealed that metal transfer took place across boundaries. Spectrum analysis on the mild steel portion near the interface (Figure 4-18a) revealed 64 wt.% of Fe and 36 wt.% of Cu; similarly, spectrum analysis on the Cu portion (Figure 4-18b) revealed 42 wt.% of Fe and 58 wt.% of Cu. Thus, the clad and substrate material at the interface boundary region is comprised of an intimate mix of both elements, and as one moves far away from the boundary, wt. % of other materials goes on decreasing, which was also observed in

EDS mapping. Spectrum of the intense mixing zone, i.e., below the nugget (Figure 4-18c) revealed the presence of equiv.-weight % of both elements.

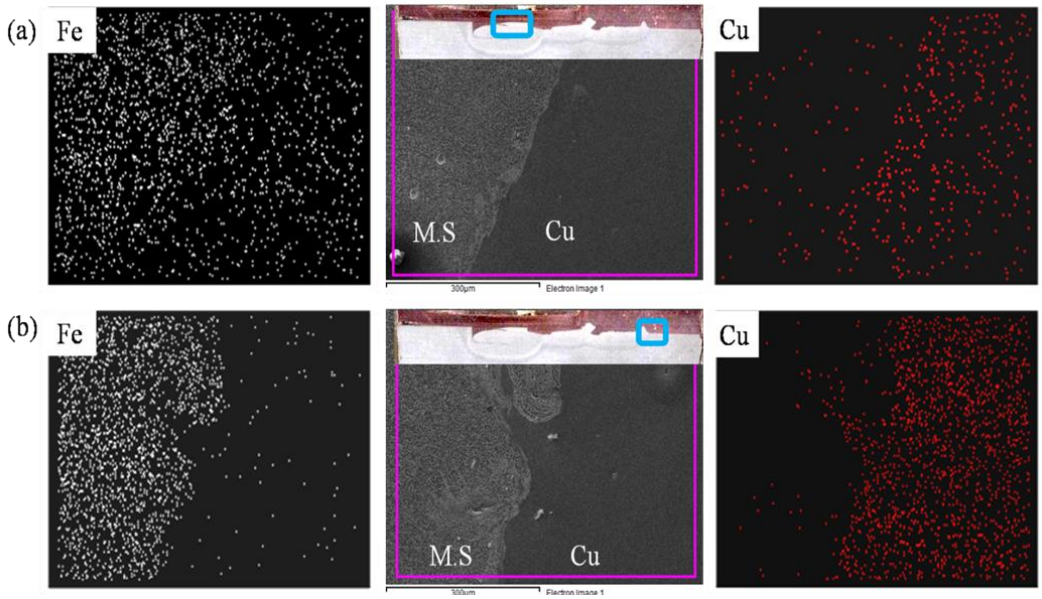

Figure 4-19 EDS mapping of transverse cross section of copper clad steel for triple pass at indicated locations

EDS mapping of different locations is shown in Figure 4-19, and it confirms that the adjacent area near the interface has undergone metal distribution across the boundary. It also confirmed that in regions away from the interface, the intensity of mixing goes down, and pure clad and substrate material are present in regions sufficiently far from the interface.

4.6 Tool offset distance optimisation

With the aim of achieving higher productivity, the largest possible tool offset distance was estimated, as this could lead to cladding in the shortest time. As mentioned in section 3.4.4, experiments were carried out with tool offsets of 6, 8, 10, and 12 mm, respectively. Figure 4-20 shows the schematic diagram showing the extent of overlap with different offset conditions. Figure 4-20a shows a higher offset distance of 12 mm,

while Figure 4-20b shows overlap with a smaller tool offset of 8 mm. Figure 4-20a reveals that with large tool offset, it results in several unbonded regions, while optimum offset offers proper bonding as shown in Figure 4-20b. The optical micrographs of the transverse clad interface with variations in offset distance are presented in Figure 4-21. It can be observed from the micrographs that, with a larger offset distance of 12 mm, a superficially bonded area remained between two successive passes with a continuous oxide layer interface (Figure 4-21a). While, with an offset of 6 mm or 8 mm, adequate overlapping arose across, as shown in Figure 4-21b with a broken oxide layer interface.

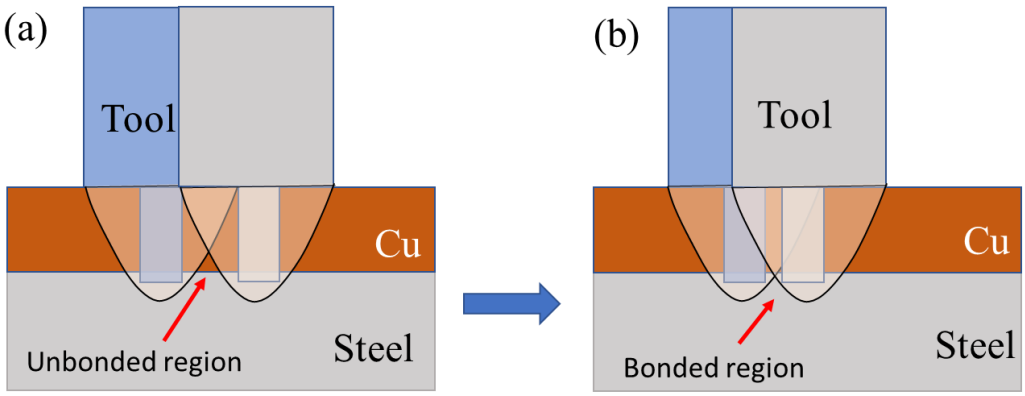

Figure 4-20 Schematic diagram demonstrating the extent of overlap (a) due to larger pin offset distance at the clad-substrate interface (b) optimum offset distance during any two successive FSW passes

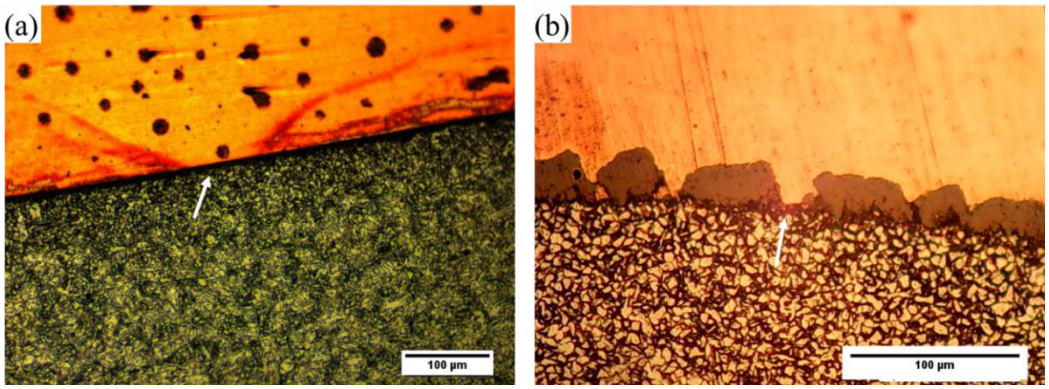

Figure 4-21 Microstructure with (a) high offset of 12 mm revealing superficial bonding along with continuous interface (b) 8 mm offset revealing broken oxide layer interface at 200X

4.7 Radiography of cladded plates

X-ray radiography images as shown in Figure 4-22 also supported the result that with an offset of 12 mm and 10 mm, some regions remained lightly bonded between two consecutive passes, as shown in Figure 4-22a and Figure 4-22b, respectively. While for an offset distance of 6 mm, as in Figure 4-22d, the overlapping region was significant, and for an 8 mm offset distance, the overlapped region just initiated, as visible from Figure 4-22c. The welds were ended at different locations to clearly represent the pinholes that are left after friction stir cladding.

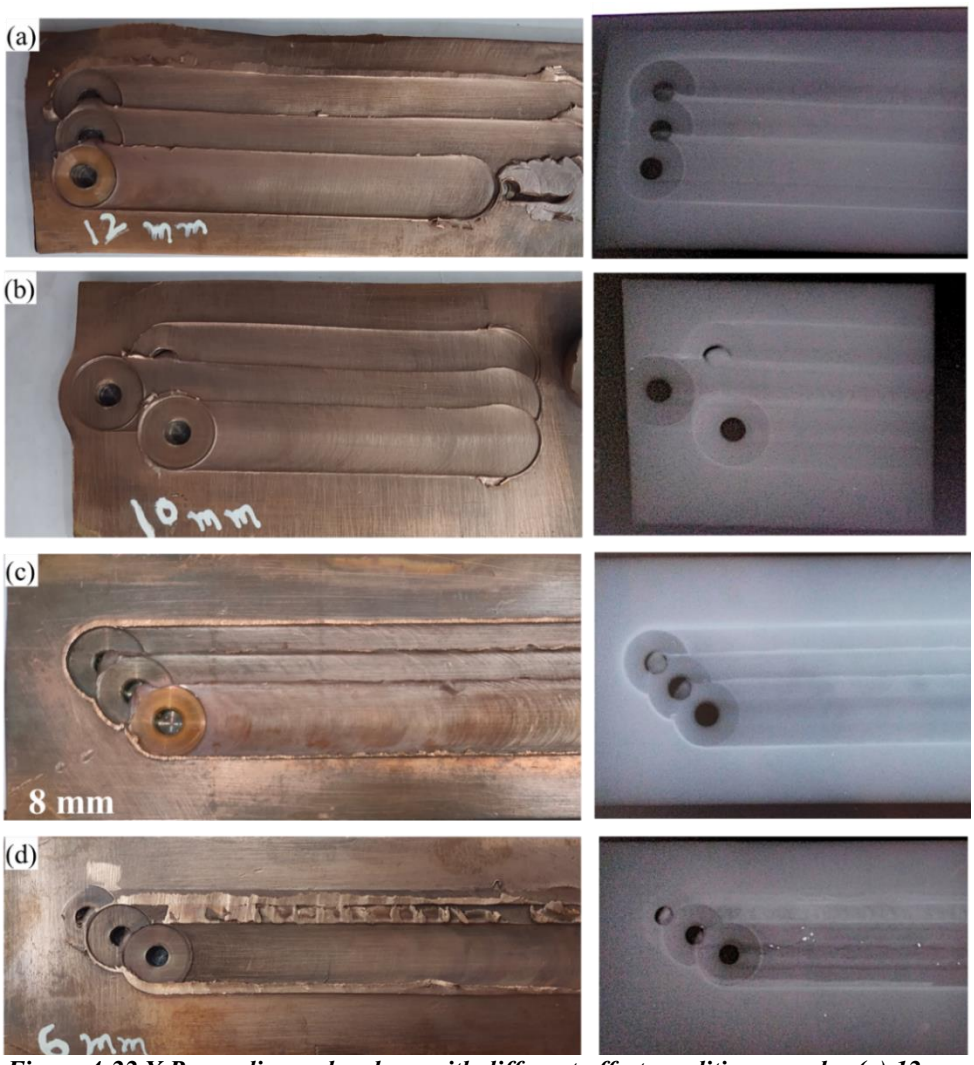

Figure 4-22 X Ray radiography along with different offset condition samples (a) 12 mm offset distance (b) 10 mm offset distance (c) 8 mm offset distance (d) 6 mm offset distance

Based upon the observation of radiography and optical microscopy, an inference was drawn that a 6 mm offset has sufficient overlapping distance, while an 8 mm offset leads to just the initiation of overlapping distance. Thus, a 7 mm tool offset distance was finalized for the rest of the experiments. Multiple samples with an offset distance of 7 mm were prepared with up to 4 passes; beyond that, it was not possible to perform the FSW passes because the clamps were in the way and the tool and collet had the risk of striking against the clamps.

Figure 4-23 shows the prepared samples with an offset distance of 7 mm, along with their X-ray radiography. In one of the initial trial runs, the tool pin broke down midway closer to the exit hole in the last pass. Tool pin fracture is one of the rare occurrences that occurs only because of the poor quality (large grains of WC and high cobalt content) of the tungsten carbide tool supplied by the supplier. However, when the recommended grade of tungsten carbide tool is ascertained, the process of friction stir cladding is quite reliable. Figure 4-23a shows a photograph of the failed experimental specimen. An abrupt ripple pattern is visible at the location where the tool pin broke down. In the position where the tool is retracted, a hole with a depth corresponding to the tool pin length is generally observed. However, in this case, when the pin broke midway, the exit hole was very shallow and corresponded to the remaining portion of the pin. The tool pin remained stuck in the plate at the location where it fractured. It was interesting to note that the broken pin is clearly visible in the radiography image (Figure 4-23b). The round white spot indicates the embedded pin (made of WC) stuck inside the plate, which was not visible in Figure 4-23a. Also, the location where the tool was retracted showed scattered particles of tungsten carbide during the withdrawal process, as shown in radiography (Figure 4-23b). Meanwhile, Figure 4-23c shows a photograph of a successfully clad plate without excessive flash or any other flaw and is accompanied, by an adjacent radiography image in Figure 4-23d. The radiography image in Figure 4-23d confirms the absence of any WC particles or unfilled space, as no spots are there in the processed plate. The round black circles at the end represent the tool exit mark. Thus, radiography images confirm proper bonding took place between copper and steel, and a good joint is obtained without any visible flaws or defects.

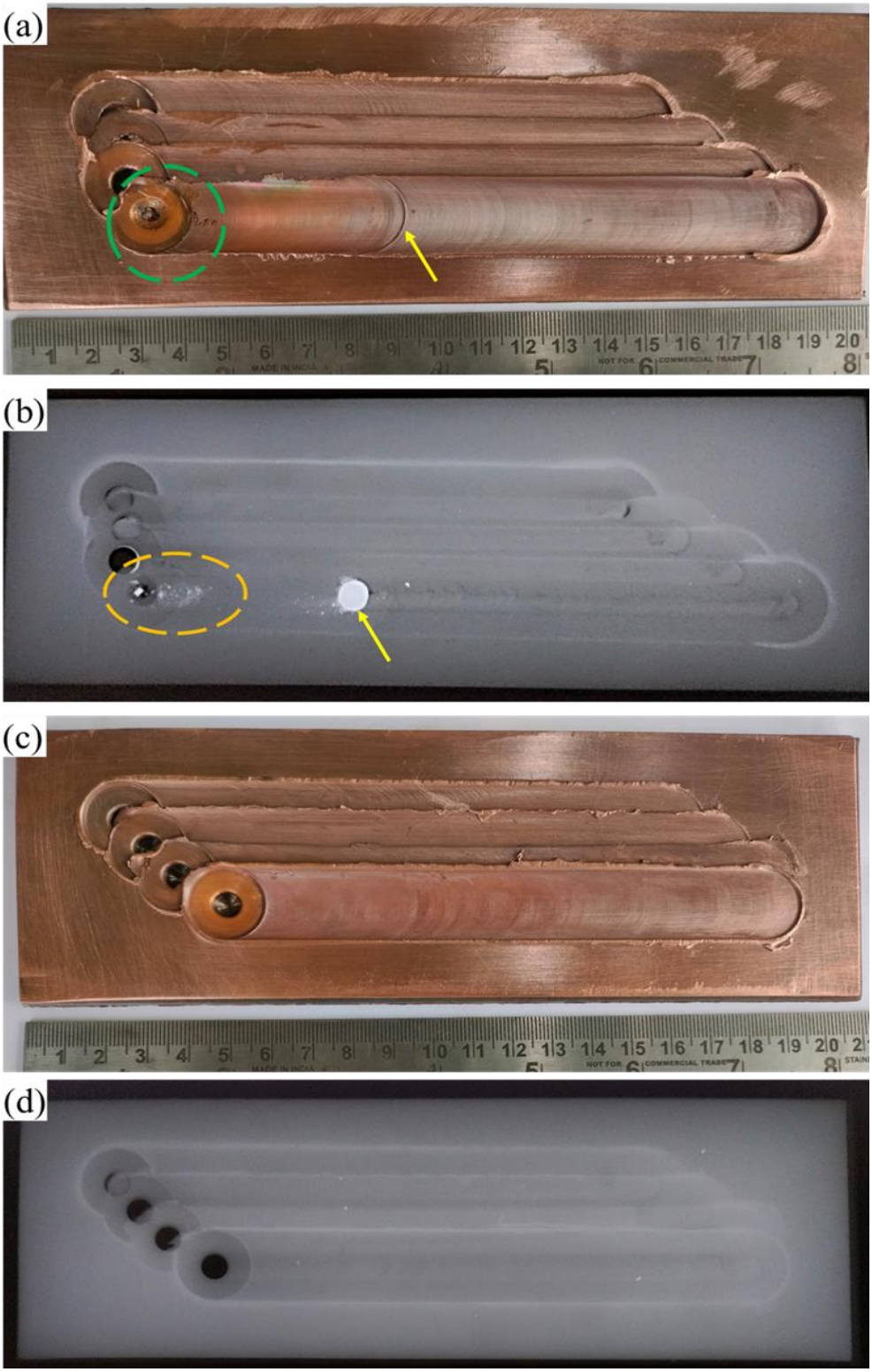

Figure 4-23 Prepared samples demonstrating (a) flaw in cladded plate (b) radiography of same sample shown in fig. a showing entrapped tungsten carbide inside (c) sample without any flaws, (d) radiography of sample shown in fig. c without any flaws

4.8 Metallography of optimised offset distance (7 mm) cladded samples

Optical microscopy was carried out on the transverse cross section of samples prepared with an optimised offset distance, i.e., a 7 mm tool offset. Figure 4-24 shows the optical images of the transverse cross section of copper clad steel. The macrograph shown in Figure 4-24 has been suitably marked to show the locations from which the micrographs have been captured. Two distinct zones are observed in the steel region, which suggests that the steel substrate has undergone plastic deformation and recrystallization up to a certain depth under the action of the rotating pin.

Figure 4-24a shows the microstructure of the base steel region, which is comprised of larger grains with an average grain size of 12 microns, while the plastically deformed portion of the substrate, as seen in Figure 4-24b has an average grain size of 5 microns. The intense stirring and heating caused dynamic recrystallization near the interface, resulting in the formation of fine grains. Similar results have also been reported by Shen et al. during the fabrication of copper-clad steel by FSW, where the average grain size near the interface remained below 5 μm [28]. Also, Guo et al. obtained similar refined grains during the friction stir additive manufacturing of copper-steel bimetallic sheets [173]. Figure 4-24b also shows the region near the interface with a wavy pattern being observed due to Kelvin Helmholtz instability resulting in wave-type motion across the interface during FSW, due to velocity shear between two layers of materials with different densities. Figure 4-24c shows the steel substrate region, which is in contact with the highly deformed copper surface with no traces of the oxide layer near the stir zone. While Figure 4-24d shows the tail of the copper region penetrating the steel substrate. Figure 4-24(e and f) depicts the region where steel is interlocked

between the copper region due to the stirring action of the tool pin, resulting in the dislodging and distribution of contact material. Also, traces of broken oxide layer are been observed in Figure 4-24e while a short range oxide layer is being observed in Figure 4-24f, stretching up to a few microns in steel. Comparison of optical images of optimised offset distance-cladded samples with those obtained by giving a 3 mm offset suggests nearly similar bonding efficiency and strong interlocking near the interface, despite the difference in tool offset. The 7 mm offset samples depicted locations without a long continuous oxide layer, as it was visible in the 3 mm offset samples, below the tool shoulder region. Thus, good bonding was obtained despite the diverse physical and metallurgical properties of copper and steel.

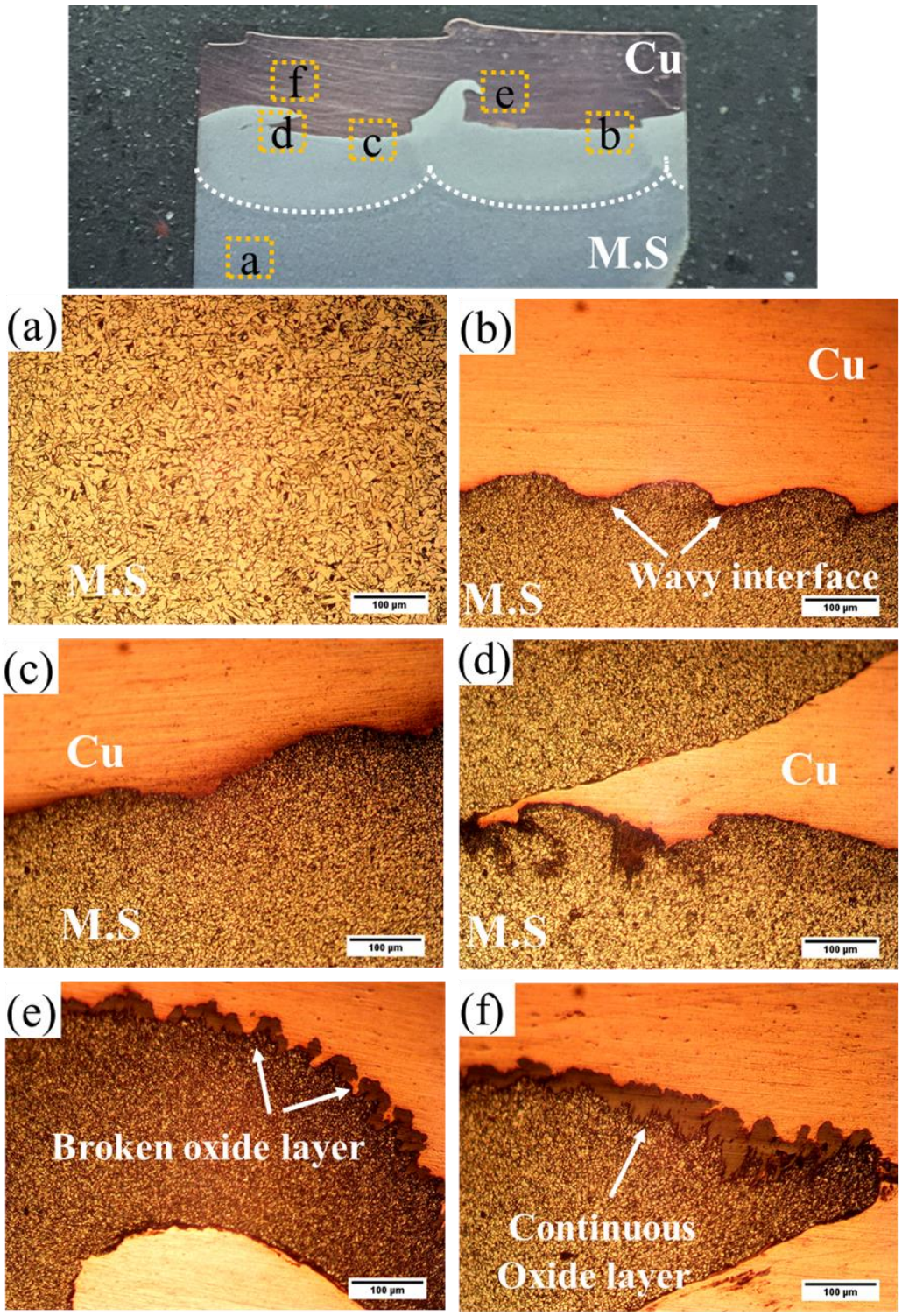

Figure 4-24 Optical microstructure of cross section (a) base steel (b) image showcasing wavy profile near the copper steel interface (c) interface below tool pin surface without any oxide layer (d) copper tail penetrating steel substrate (e) bounded steel region with broken oxide layer (f) steel region penetrating copper area

4.8.1 Optical microstructure of concurrently etched clad specimen

With all the initial attempts, it was only possible to etch either the steel substrate or the copper-clad region at a time, but attempts were rigorously made to etch the entire cladding concurrently. This was felt to be very essential to evaluate the bonding interface more precisely and to have a more detailed insight into several aspects of clad through optical and SEM images. After several attempts, intermittent etching the entire clad with a mixture of 10 parts HCl and 1-part nitric acid for 1 minute, followed by re-etching again for 1 minute, proved to be beneficial in revealing the microstructure of both the clad layer and the substrate in the cladded specimens concurrently.

The optical images of the transverse cross section of a clad have been shown in Figure 4-25, where both copper and steel have been etched concurrently. The macrograph of the site consists of similar hook like features, separated by a distance of 7 mm, i.e., the offset distance, which confirms tool plunge parameters were identical for all passes. Also, due to the usage of a 4 mm pin length, i.e., 1 mm longer than the clad plate thickness, this type of appearance, i.e., encroaching of material on each other, is being observed at the sites where the tool pin pierces through the clad layer and moves into the substrate material. Figure 4-25a shows the base steel region, while Figure 4-25b shows the microstructure of base copper with an average grain size of 18 microns. The region near the clad interface has been shown in Figure 4-25c, demonstrating etched regions of both. The stir regions comprised refined grains of steel near the interface with grain sizes of approximately 5 microns, while the copper portion comprised refined grains of nearly 10 microns adjacent to the interface, while grains away from the interface measured around 20 microns. Similar results have also been obtained by

Sasaki et al., where copper grains were slightly finer near the copper-steel interface than those away from the interface [42]. Grain coarsening was observed for the majority of copper grains due to the multipass action, i.e., repeated stirring. The interface region shows proper bonding between the two. Figure 4-25d shows the location where copper was found penetrating into the steel portion, and several branches can be observed originating from the copper region, which suggests strong mechanical interlocking between the two. Figure 4-25e shows the portion where the flow of material near the interface has been demonstrated due to tool stirring and depicts the microstructure of the same location as indicated in the macrograph. Similarly, Figure 4-25f shows the location where the steel region got entrapped between the copper boundary due to the high flowability of copper. Thus, based on optical microscopy, it can be concluded that strong interlocking and material distribution were observed near the stir zone, which is also visible from the macrograph, and grain refinement was observed near the interface for the steel substrate region.

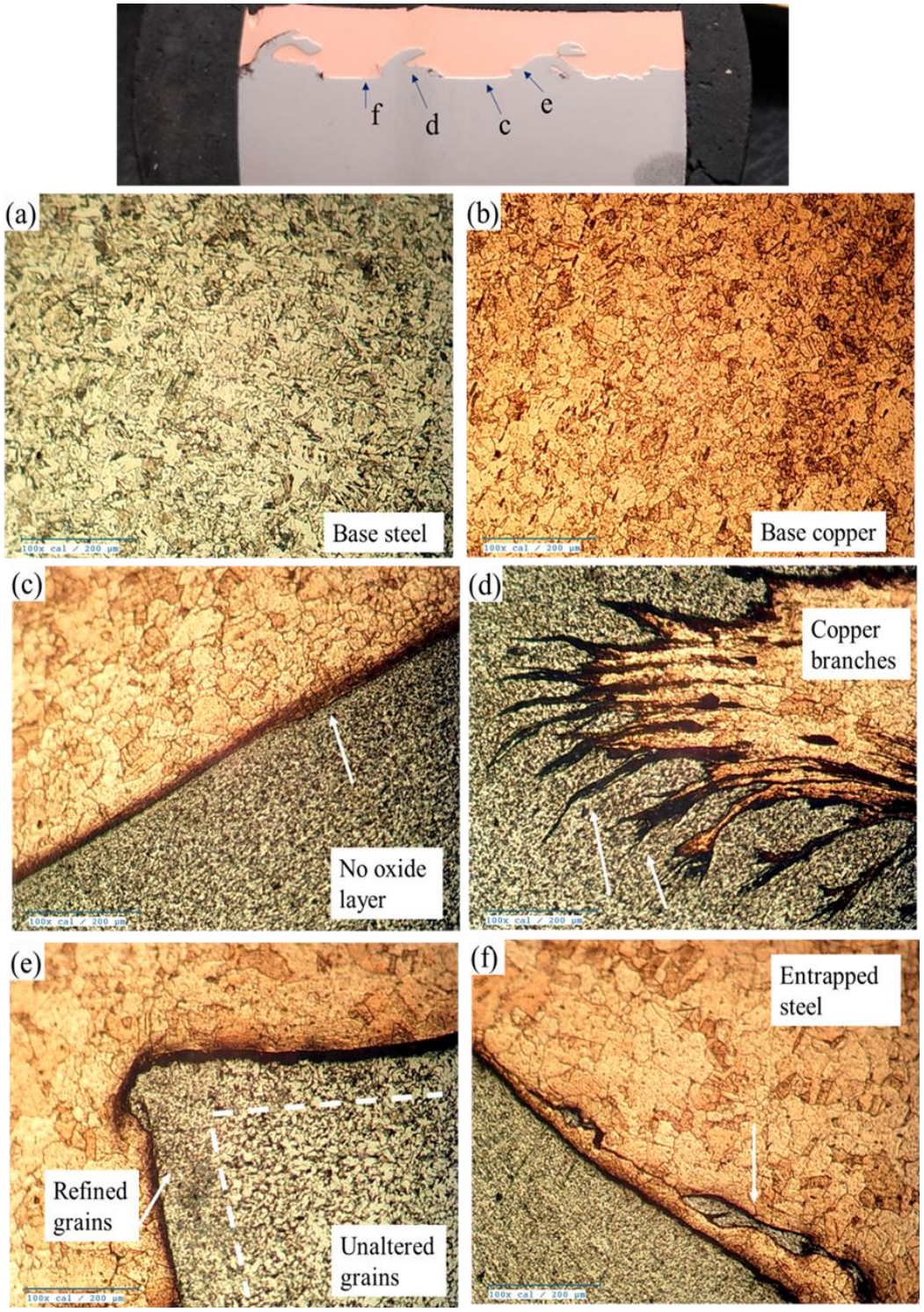

Figure 4-25 Optical microstructure of transverse cross section (a) base steel (b) base copper (c) interface region near stir zone demonstrating grain refinement in steel substrate without oxide layer (d) copper branches penetrating steel surface (e) region showcasing unaltered and refined grain zones of steel (f) location with engulfed steel portion

4.8.2 SEM analysis of the concurrently etched specimen

SEM analysis, carried out for the concurrently etched sample with an optimum offset of 7 mm around the interface region, has been shown in Figure 4-26. Figure 4-26a depicts the portion where copper branches are penetrating into the steel substrate, suggesting proper bonding and mechanical interlocking without any void formation. Similarly, Figure 4-26b shows another portion of the bonded region that demonstrates the flowability of copper near the interface under the action of a pin, which takes the shape of a hook, leading to visibly strong bonding between the clad and substrate materials. Figure 4-26c shows the region where copper is entrapped between adjacent steel regions. The wavy pattern-type appearance in Figure 4-26d was observed over several microns near the nugget interface. Figure 4-26e shows the interface boundary region at high magnification, suggesting proper bonding without any oxide layer in between the clad and substrate. Similarly, the microstructure of the cladded interface has been shown in Figure 4-26f, where a high degree of mechanical interlocking causes superior bonding between the clad and substrate.

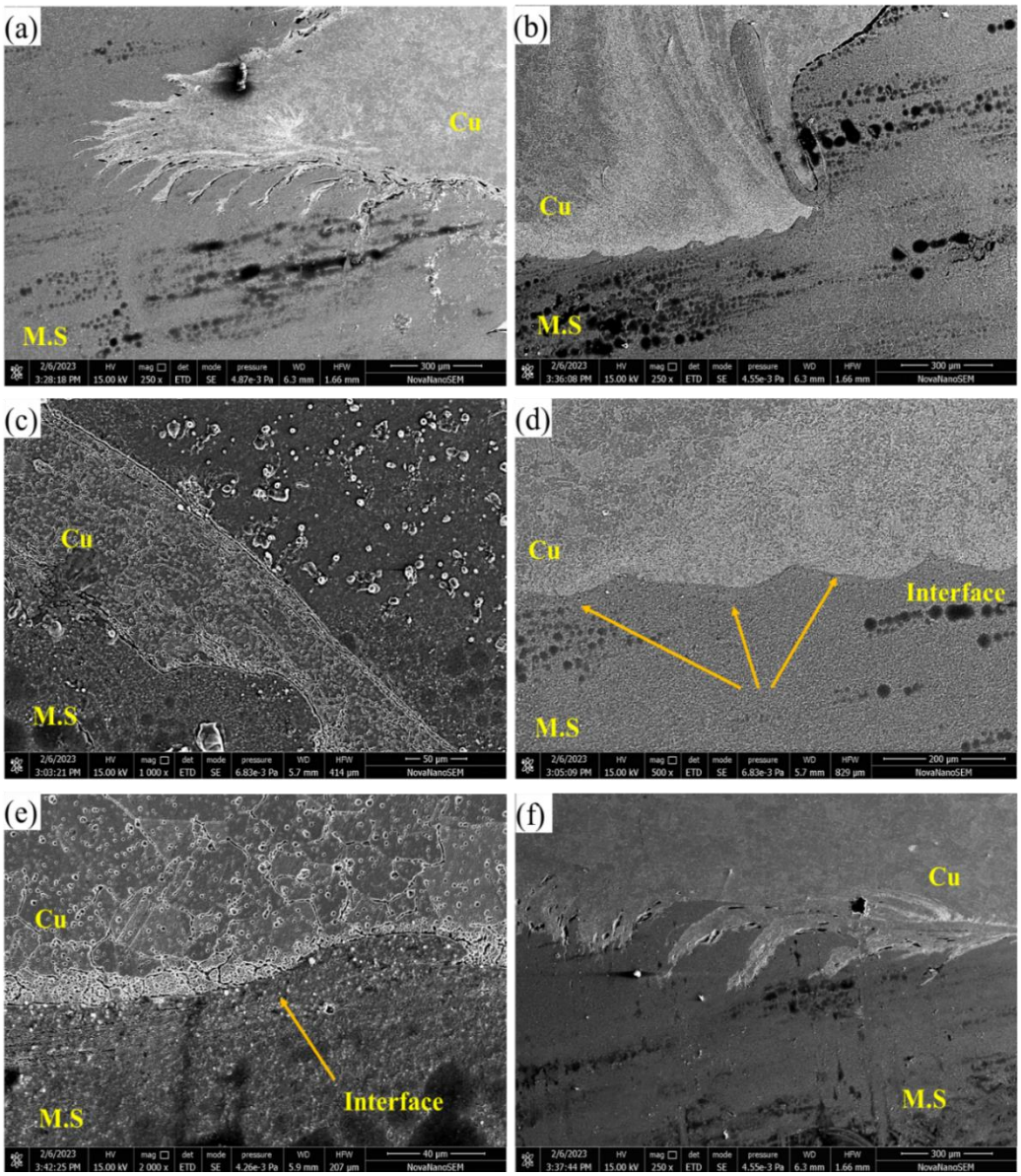

Figure 4-26 SEM images of clad interface demonstrating (a) copper branches penetrating steel region (b) region near interface demonstrating hook type feature (c) region with copper in between steel portions (d) wavy profile near stir region (e) magnified view of steel copper interface (f) interface demonstrating mechanical interlocking

Figure 4-27 shows an EDS map of the transverse section of the cladded region. The SEM image of the interface is shown in Figure 4-27a. The EDS mapping for copper is presented in Figure 4-27b while Figure 4-27c shows the EDS map for steel. The two images show the respective regions without any oxide layer between them. Slight dispersion of the opposite material near the interface indicates cross boundary metal

transfer, which has also been reported to be useful by Jamaati et al. for interfacial bonding strength [133]. The map EDS results shown in Figure 4-19 seems to have larger diffusion, while Figure 4-27 shows considerably less diffusion. The probable reason for this appearance could be attributed to the fact that the prior result in Figure 4-19 was obtained when the tool pin offset was not optimised, i.e., 3 mm, which suggests the offset distance was very low for cladding. Due to the very low offset, there was considerable stirring of material, and this considerable stirring led to more cross-boundary diffusion. The samples used for EDS in Figure 4-27 have been obtained after the optimised offset distance of 7 mm. This fact resulted in less cross-border metal diffusion due to the occurrence of stirring taking place at a larger offset distance between two adjacent passes. This further proved that the optimised offset distance would also ensure lesser diffusion.

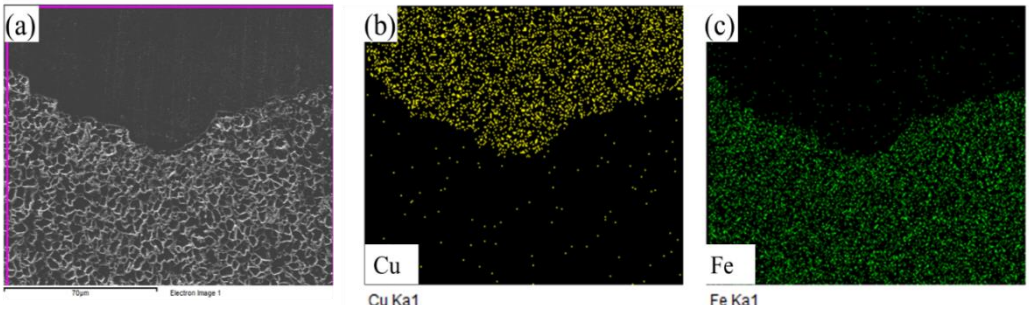

Figure 4-27 SEM images (a) near interface (b) EDS map of copper (c) EDS map of steel

Figure 4-28 shows the EDS quantification of a spot near the stir zone. Spot A is on the steel region and shows Fe 55% and copper 44%, which is in support of the fact that material intermixing took place with cross-border metal transfer near the interface. Similarly, site B is in the copper region, and EDS quantification shows the dominance of copper in that region, with copper at 68% and Fe at 31% with cross-border metal transfer, which enhances the strength of the bimetallic clad.

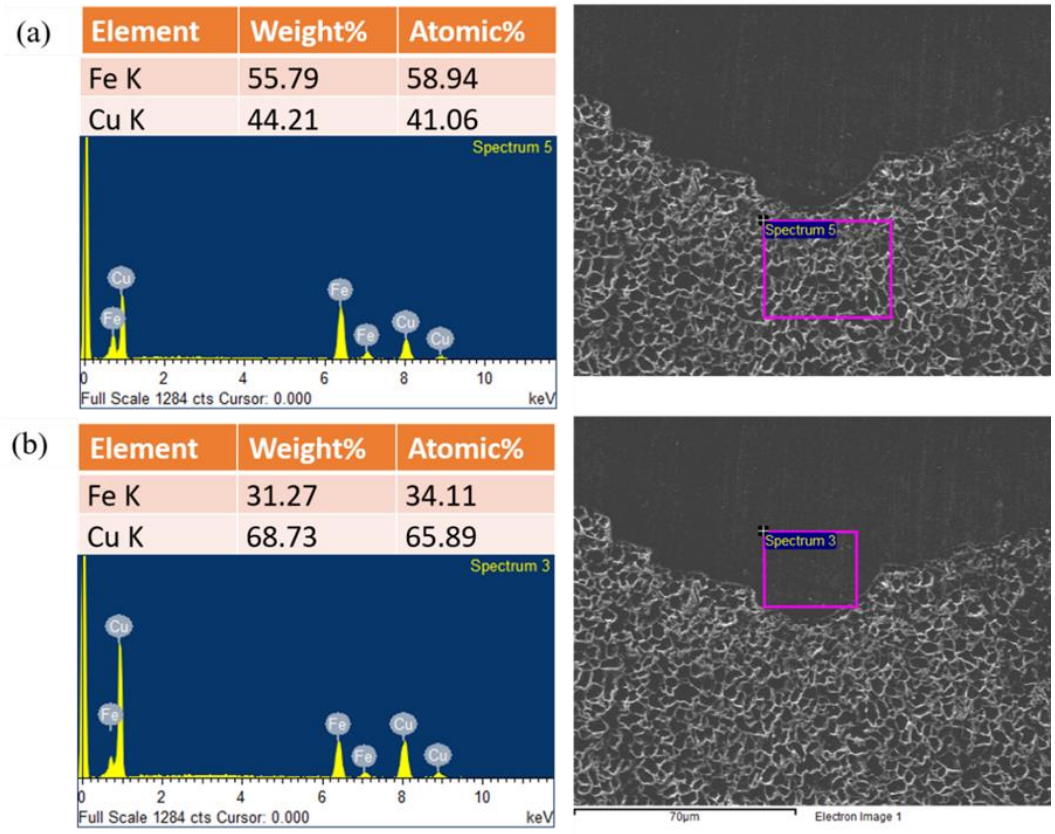

Figure 4-28 EDS quantification of location near interface (a) steel region (b) copper region

4.9 Tensile results of cladded samples

Tensile samples have been extracted from the cladded region of copper clad steel samples and have already been shown in Figure 3-10 in the experimentation section. Cladded specimens undergoing necking during tensile testing have been shown in Figure 4-29a, and the fractured samples of as-received copper, as-received substrate (steel), and copper clad steel with a 6 mm final thickness have been shown in Figure 4-29b. The physical appearance of the cladded sample shows no delamination.

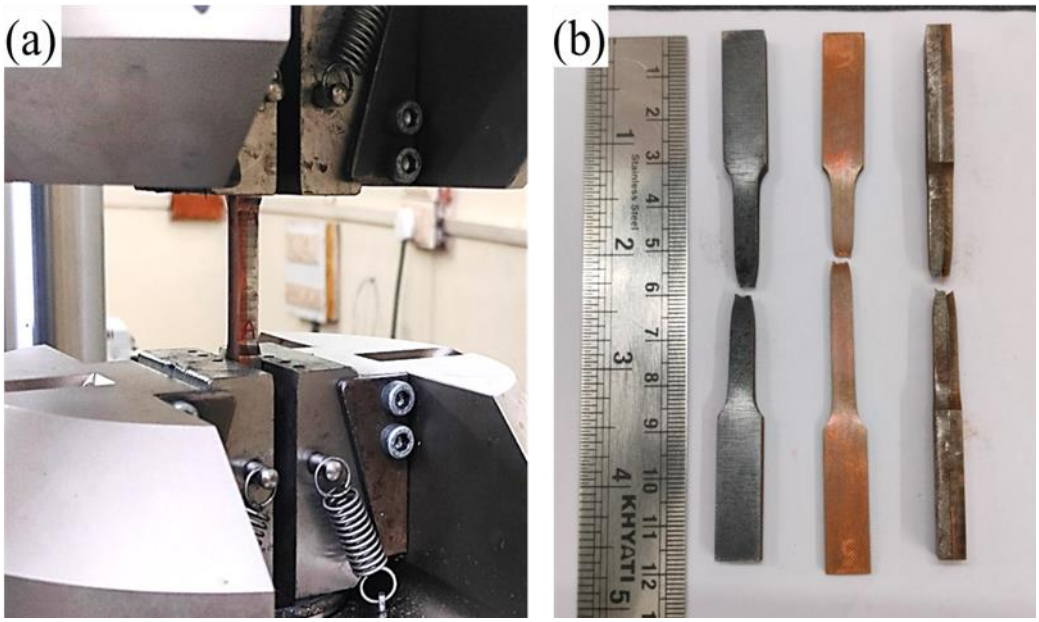

Figure 4-29 Demonstration of (a) necking phenomena in cladded sample (b) fractured tensile samples

The engineering stress-strain curves of as-received copper, steel, and clad samples are shown in Figure 4-30. The copper specimen shows no prominent yield point, while the mild steel substrate and the cladded plate demonstrated the yield point phenomenon. It was observed that the yield strength and UTS of cladded material fall between those of as-received copper and steel. The result agrees with the results of Guo et al., where the author prepared a similar copper steel bimetallic sheet by friction stir additive manufacturing of 6 mm thickness and obtained comparable results for the joint. They also claimed that, compared to a copper substrate, the copper steel bimetal joint obtained great improvements in tensile properties, suggesting a sound joint at the interface [173]. Similarly, Liu et al. prepared copper clad steel plates through cold rolling and obtained YS and UTS of 261 MPa and 335 MPa, which are very similar to the obtained results in this study [45]. The clad material shows lesser ductility in comparison to both parent materials. This can be attributed to the formation of

intermetallics at the interface, due to which the reduced ductility of the clad is observable.

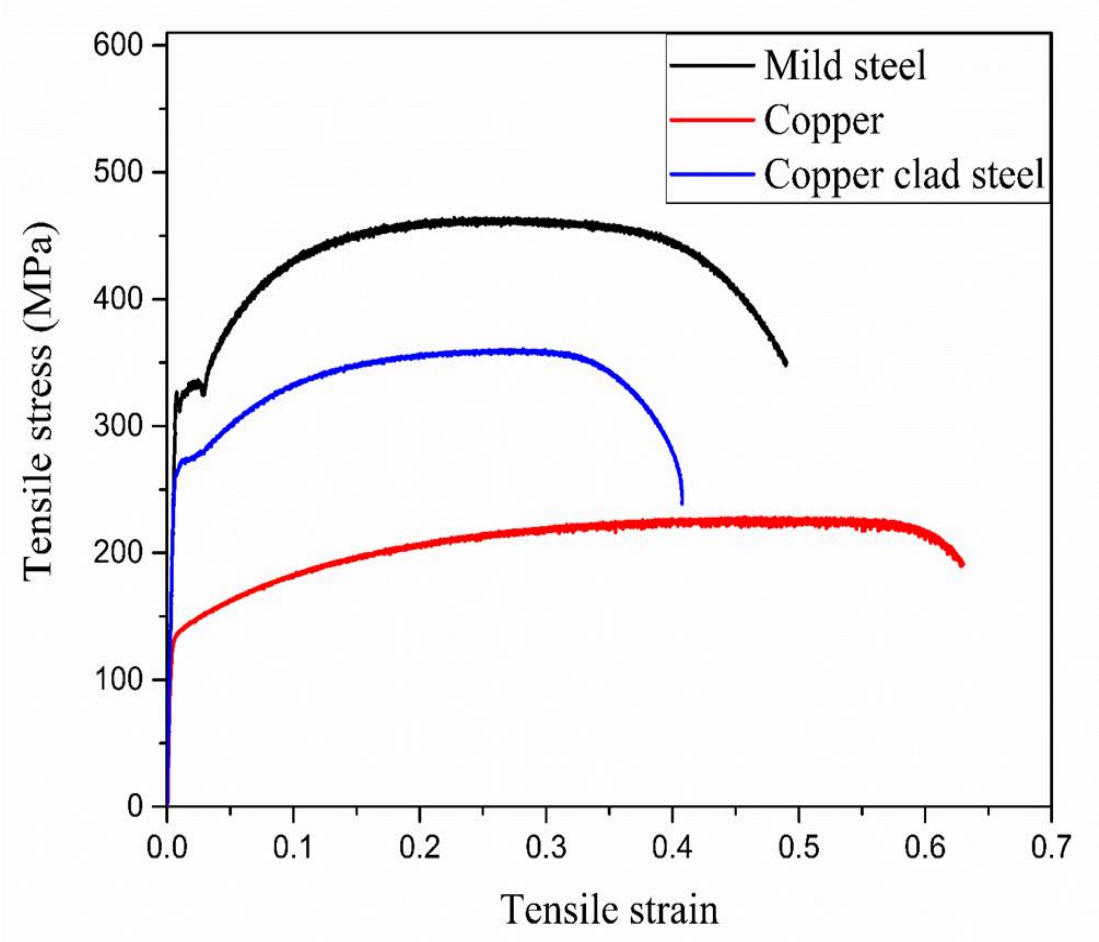

Figure 4-30 Stress strain graph comparing the tensile properties of copper, steel, and cladded bimetal joint

Figure 4-31 compares the tensile properties of as-received copper, steel, and copper clad steel, respectively. The received copper has an YS of 131 MPa, an UTS of 227 MPa, and an elongation of 67.6 percent, which is comparable with the standard data [215]. Similarly, the mild steel used in this work has a YS of 326 MPa and a UTS of 462 MPa and shows an elongation of 50 percent. The percentage elongation measured is slightly higher than that reported for typical mild steel. The elongation of mild steel is dependent on the carbon content, and in this case, carbon content of AISI 1018 steel

was on the lower side (0.17%). Therefore, the higher elongation can be attributed to the low carbon content of AISI 1018 steel. The other factor that could have caused the increased elongation is that a low strain rate was used during the tensile testing. Additionally, no extensometer was used to record the elongation of the gauge portion; consequently, the elongation value reported is approximate. The YS of copper clad steel has a YS of 261 MPa and a UTS of 359 MPa, which is higher than as-received copper but lower than steel. The clad joint demonstrated an elongation percent of 40.9, which is lower than the elongation of both as-received copper and steel. Compared with as-received copper, the copper cladded steel obtained a great improvement in tensile properties, suggesting a sound joining at the interface.

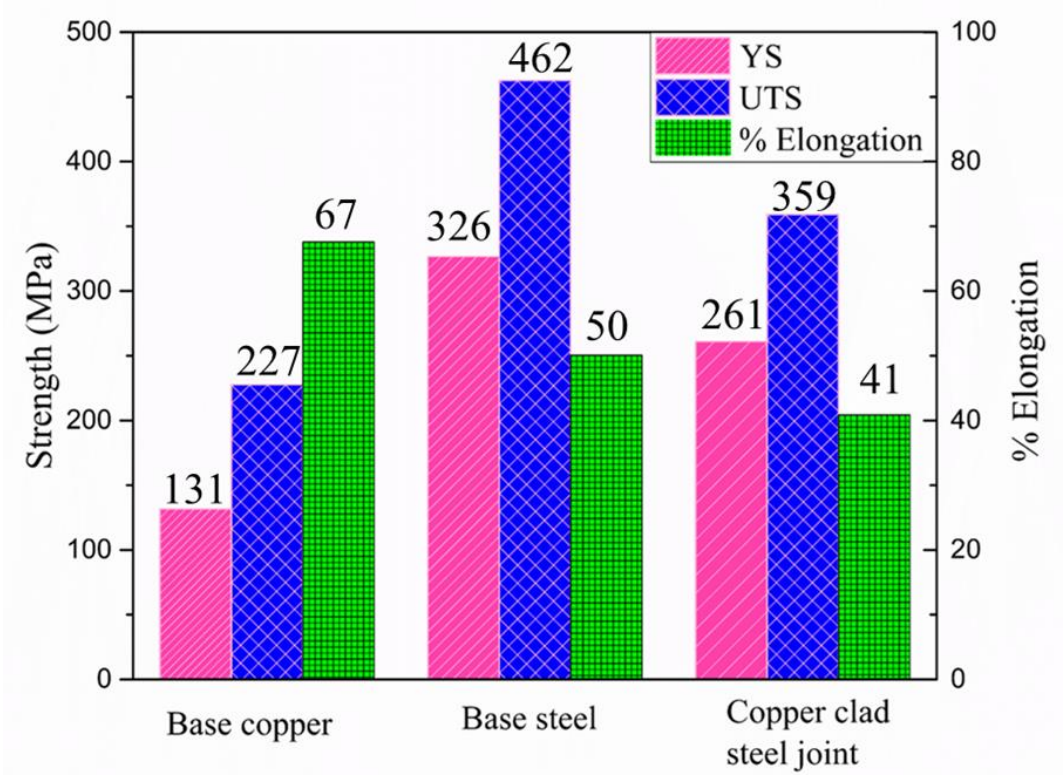

Figure 4-31 Comparison of tensile properties (YS, UTS, and % elongation) for base copper, mild steel, and copper clad steel

4.10 Fractography of cladded samples

The fractography of the as-received materials and clad samples has been carried out. Figure 4-32(a and b) show the fractography images of as received copper and steel, respectively. Fractography of copper reveals typical features obtained in copper. A large number of deep dimples can be seen, implying entirely ductile fracture behaviour, while fractography of the as received steel demonstrated shallow dimples of uniform sizes. Figure 4-32c depicts the images of fractured surfaces obtained on the cladded samples. The interface appears to have a narrow opening, which might be due to the difference in the amount of stretching between copper and steel. Figure 4-32d and Figure 4-32e shows the interface region at low and high magnification, respectively. The fractured copper region shows the presence of larger dimples. Due to the diffusional interface, the bonding between the layers in the samples was preserved, and they fractured almost as a single piece of material.

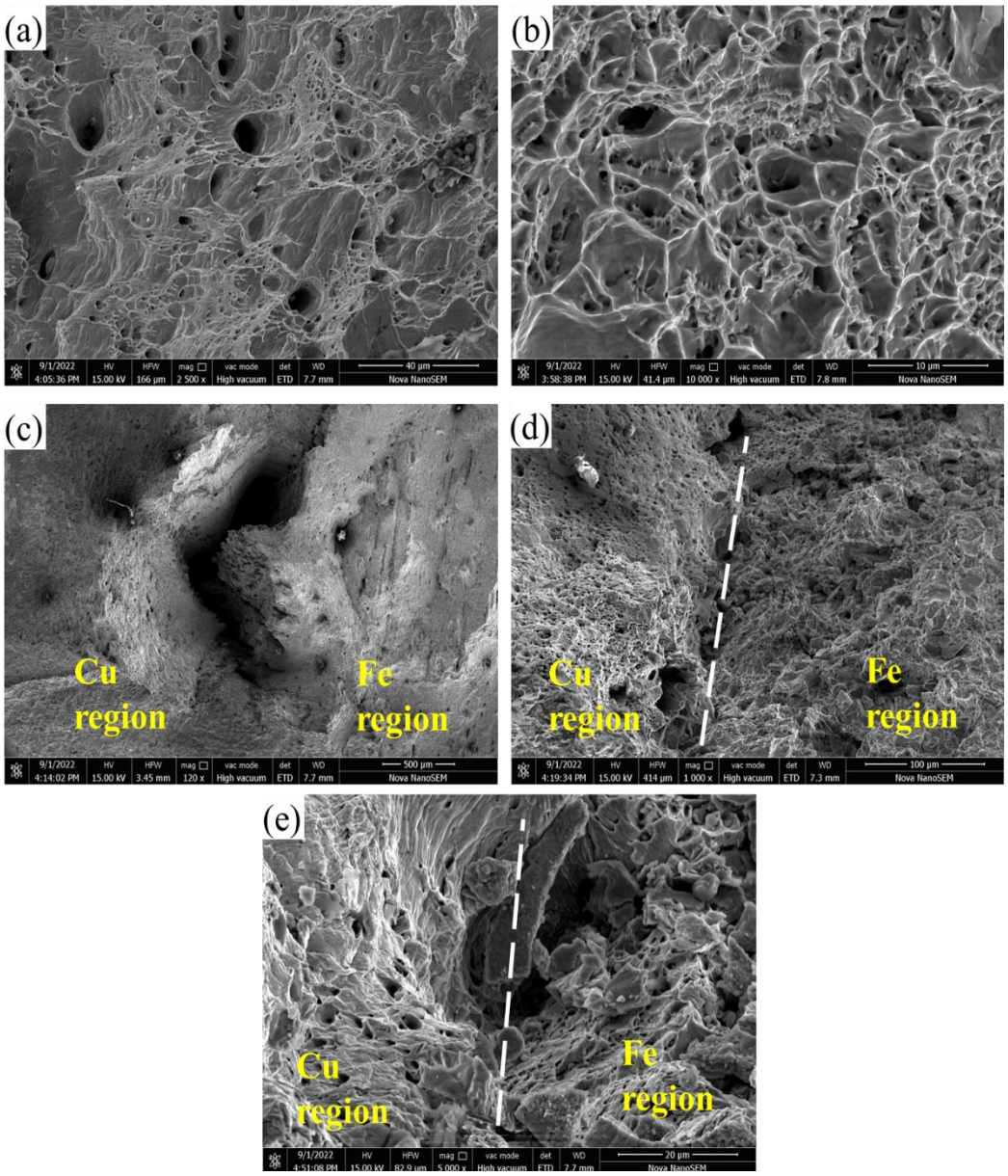

Figure 4-32 Fractography images for (a) received copper (b) received mild steel (c) copper clad steel fractured face portion (d) interface fractured surface (e) enlarged copper steel interface showing dimples in copper

Figure 4-33a shows the fractured surface of the interface of a cladded tensile sample, with the copper region comprising dimples on the left while the steel surface is shown on the right. Figure 4-33b and Figure 4-33c represents the EDS maps of copper and steel, respectively. Figure 4-33d shows the elemental distribution of both constituent materials, confirming that diffusion transfer of elements took place across the boundary near the interface.

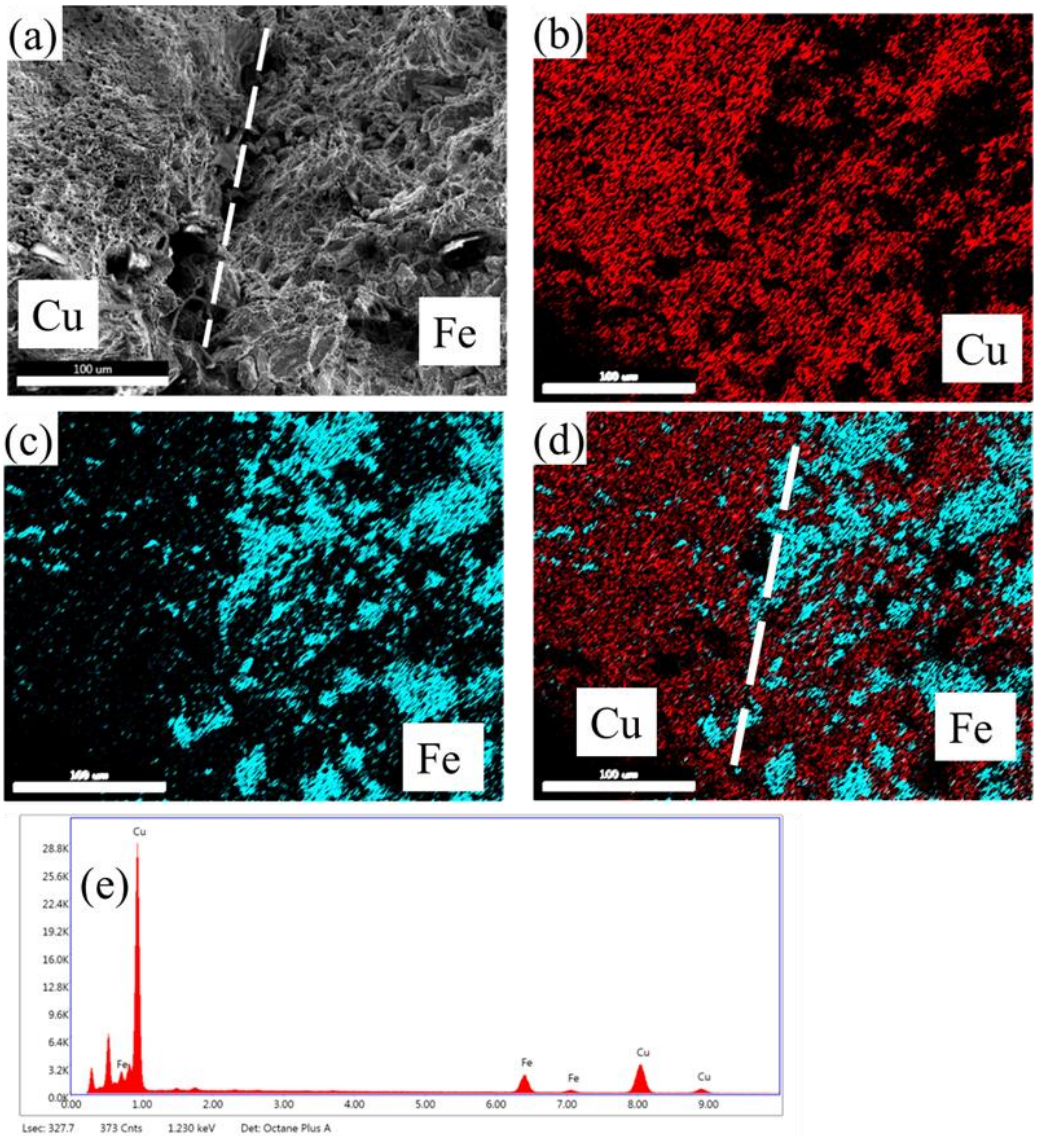

Figure 4-33 (a) SEM image of fractured interface region (b) EDS map of copper distribution (c) EDS map of steel distribution (d) EDS map of both constituent materials overlaps (e) EDS spectra of copper and steel interface

The gauge portion of tensile test specimens was observed at various magnifications to understand the deformation behaviour of the copper steel interface. Figure 4-34a shows the tensile gauge length of the clad region, while Figure 4-34b and Figure 4-34c depict the SEM image of the same. The image shows the stretching marks between copper and steel and indicates a strong bond between copper and the steel substrate. The stretching marks are assumed to be formed due to the difference in ductility between copper and steel. During uniaxial tensile testing, upon the onset of the load,

the copper region tried to elongate rapidly while the steel region resisted the elongation, resulting in the formation of the stretching marks. The excellent bonding also resulted in the failure of the cladded material at an elevated load in comparison to the as-received copper. However, the load at failure was lower than that found in the as-received steel samples. Figure 4-34c shows an enlarged view of the stretched cavity with cracks propagating from the corners. It can be confirmed that along the gauge length, cladded material is behaving as a single material. Figure 4-34d and Figure 4-34e represents the EDS maps of copper and steel, respectively. Figure 4-34f shows the EDS map of both constituent materials, confirming the existence of strong bonding near the interface boundary with cavities arising out of stretching activity due to the different elongation rates of copper and steel.

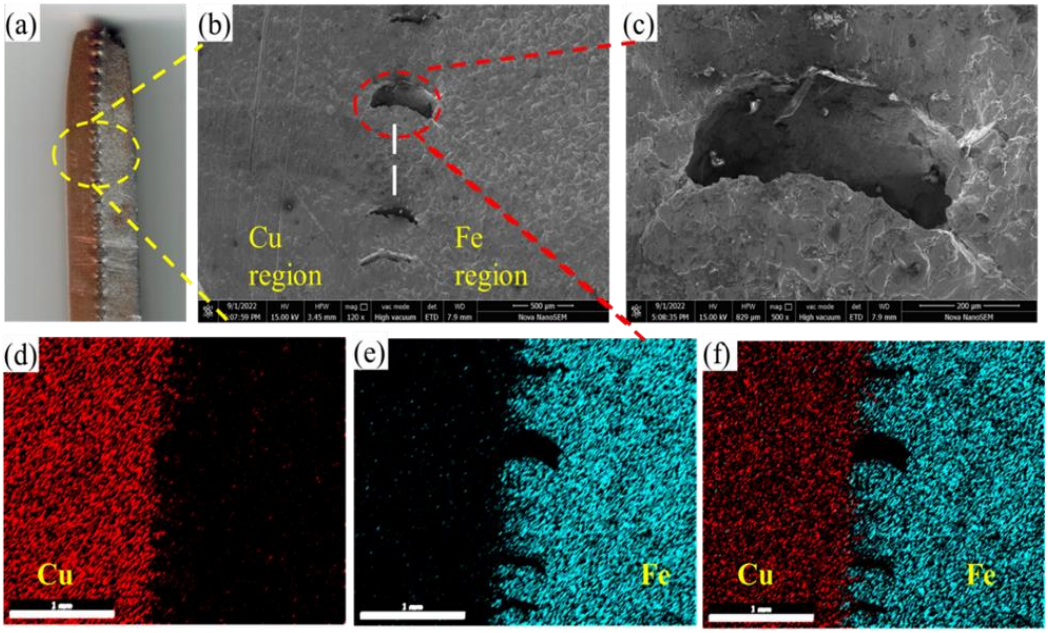

Figure 4-34 (a) Fractured tensile gauge length with stretching marks (b) SEM image of the interface region (c) SEM image of stretched cavity in enlarged view with crack propagation marks (d) EDS map of copper distribution (e) EDS map of steel distribution (f) EDS map showing both constituent materials overlaps

4.11 Guided bend test of cladded samples

The guided bend test was carried out for the determination of the soundness of joint quality in the clad region. The extracted copper clad steel samples were laid on top of rollers spaced evenly apart from each other and bent into a U shape by exerting force in the centre with the aid of a plunger. Face bend (substrate up) was carried out by placing the cladded copper portion on the bottom; root bend (substrate down) was carried out by placing a steel substrate region on the bottom surface in contact with rollers; and side bend (transverse section) was carried out by placing a copper clad steel region, i.e., joint surface, on the bottom side. Upon loading, the cladded samples were subjected to progressive localised overstressing, resulting in the formation of a U shape as shown in Figure 4-35.

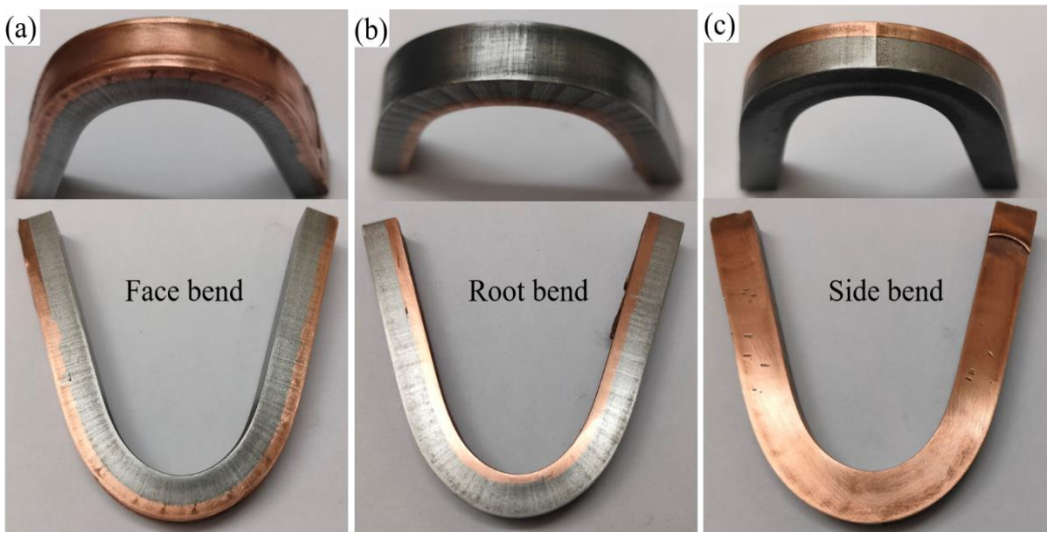

Figure 4-35 Guided bend test results (a) face bend (b) root bend and (c) side bend

The convex surface of the bend was carefully observed for cracks or any other defects. U-bends were obtained for all the cases without any noticeable cracks or flaws. The convex region shows no sign of cracks or tearing marks, while no delamination effect

was observed in the U-shaped interface region, proving the joint quality between the clad and substrate materials is satisfactory for any industrial application.

4.12 Microhardness of cladded samples

Microhardness evaluation was done throughout the transverse cross section at three different vertical heights as shown in Figure 3-9a in the experimentation section, i.e., near the top surface of copper clad, in copper close to the interface, and in mild steel close to the interface for single pass clad and multi pass clad respectively. The microhardness obtained has been shown in Figure 4-36a for single pass, and Figure 4-36b for multi pass clad.

Microhardness evaluation of the cladded sample for single pass at Figure 4-36a reveals that the hardness value of the cladded copper near the interface and near the top surface was almost the same. The difference in hardness between the advancing side and retreating side was slightly more pronounced in the copper near the interface, as shown in Figure 4-36a. The hardness values for the mild steel portion, just near the interface, revealed expectedly much higher values than the copper near the interface. Also, a greater variation in microhardness could be seen, particularly near the nugget zone, while hardness in the HAZ was more uniform and slightly lower.

Similarly, the microhardness variation for the cross section of the multi-pass clad showed no remarkable variation for the copper portion throughout its thickness as seen in Figure 4-36b. But on the steel substrate portion, it recorded a dip in average microhardness values for multi-pass. This might have taken place due to the probable dissolution of intermetallics and the reduction in dislocation density due to repeated heating. As a result, the average microhardness of the steel substrate for multi-pass

was reduced in comparison to single-pass. Microhardness variation with a 7-mm tool offset resulted in similar results and has been shown in Figure 4-37.

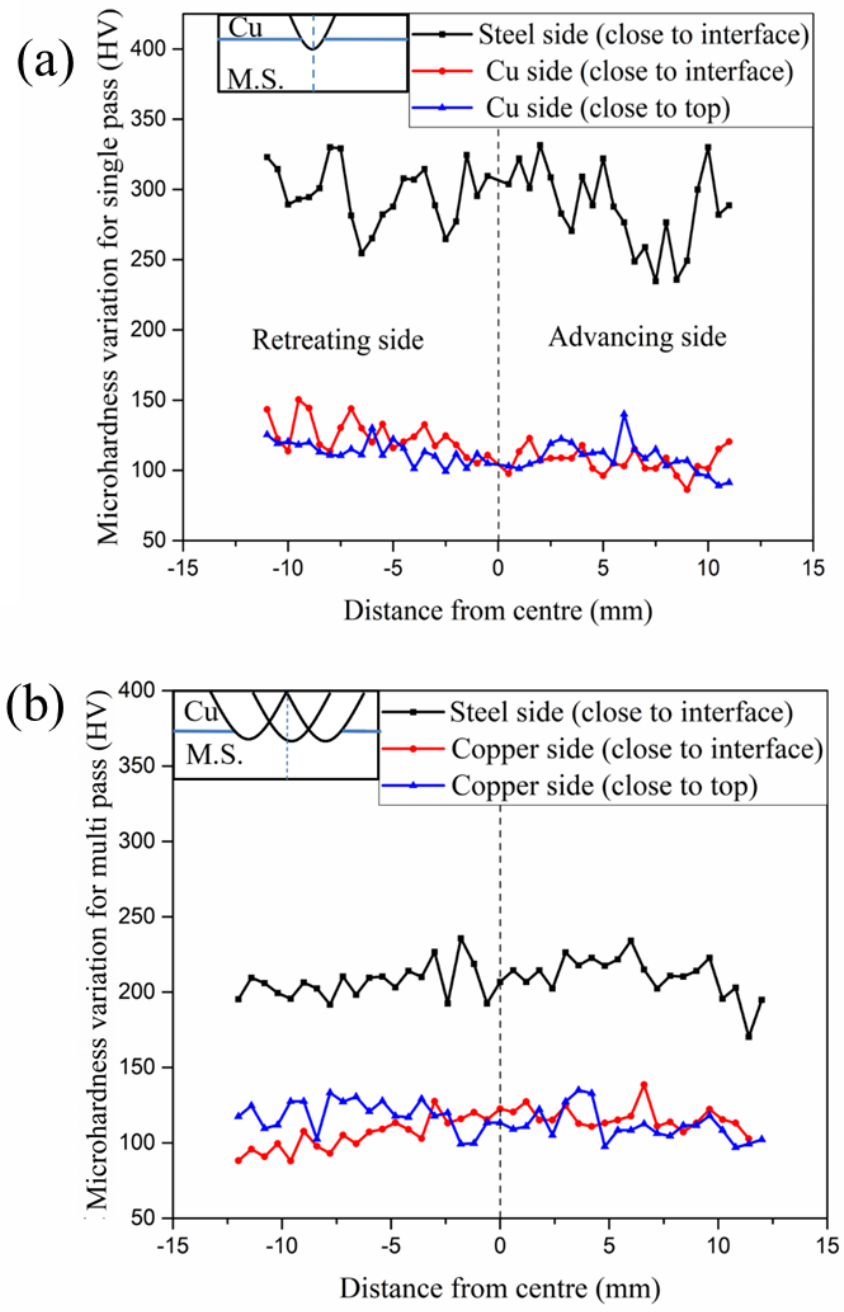

Figure 4-36 Graph showing microhardness variation for 3 mm offset at different locations for (a) single pass (b) triple passes

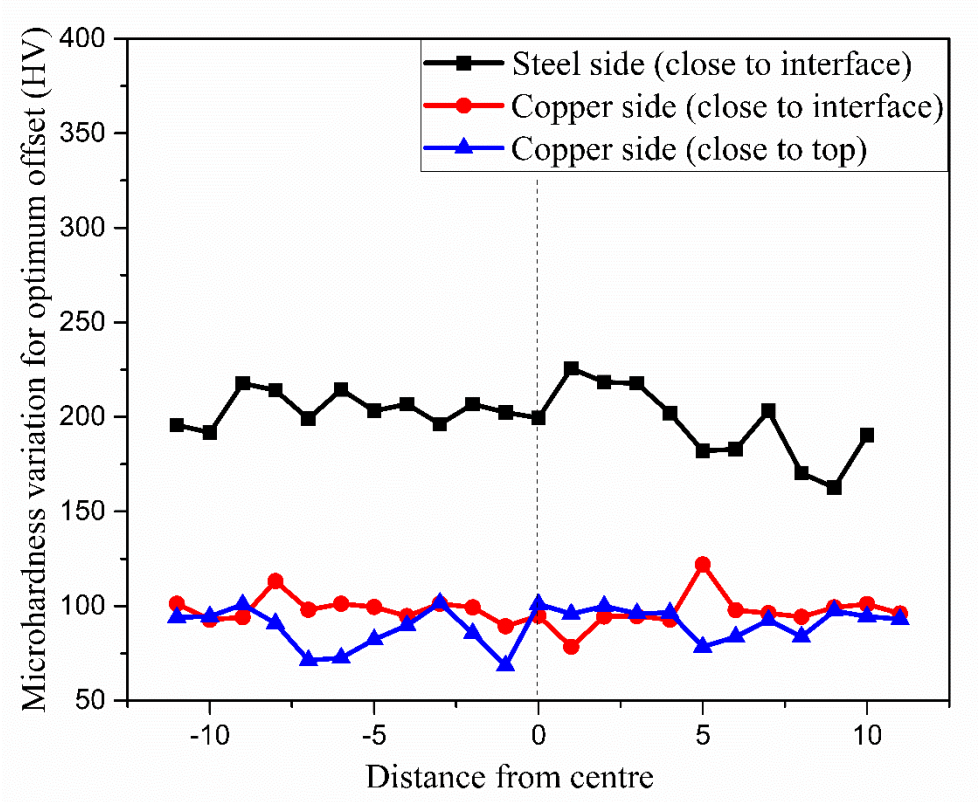

Figure 4-37 Microhardness variation with 7 mm tool offset for copper clad steel at different locations

Microhardness measurements were also carried out on the interface section from top to bottom. Indentations were taken across the transverse cross section covering the copper-steel interface region at an interval of 0.5 mm between each indentation. The results of the microhardness test are shown in Figure 4-38, and reveal that the microhardness obtained in the clad layer and the substrate were typical of those found in the respective materials. The hardness value near the interface was found to be the highest, with the hardness value reaching 226 HV due to refinement of grains near the interface, which can be justified from the fact that the initial indentation taken on the steel side is too far from the interface (nearly 100 microns). Therefore, the chances of intermetallics being present in that region are very small. Moreover, the carbon content in the substrate was very low, and the cooling rate was also not very high; therefore, martensite formation is unlikely to happen. Thus, it can be concluded that the increase

in hardness is mainly due to grain refinement. The hardness value across the steel portion gradually decreased as one moved away from the interface, as the effect of grain refinement gradually diminished. Guo et al. reported that the hardness value at the interface was the highest, caused by the refinement of crystallised grains at the interface, and the hardness value gradually decreased from the joint interface to the base material on both sides [173].

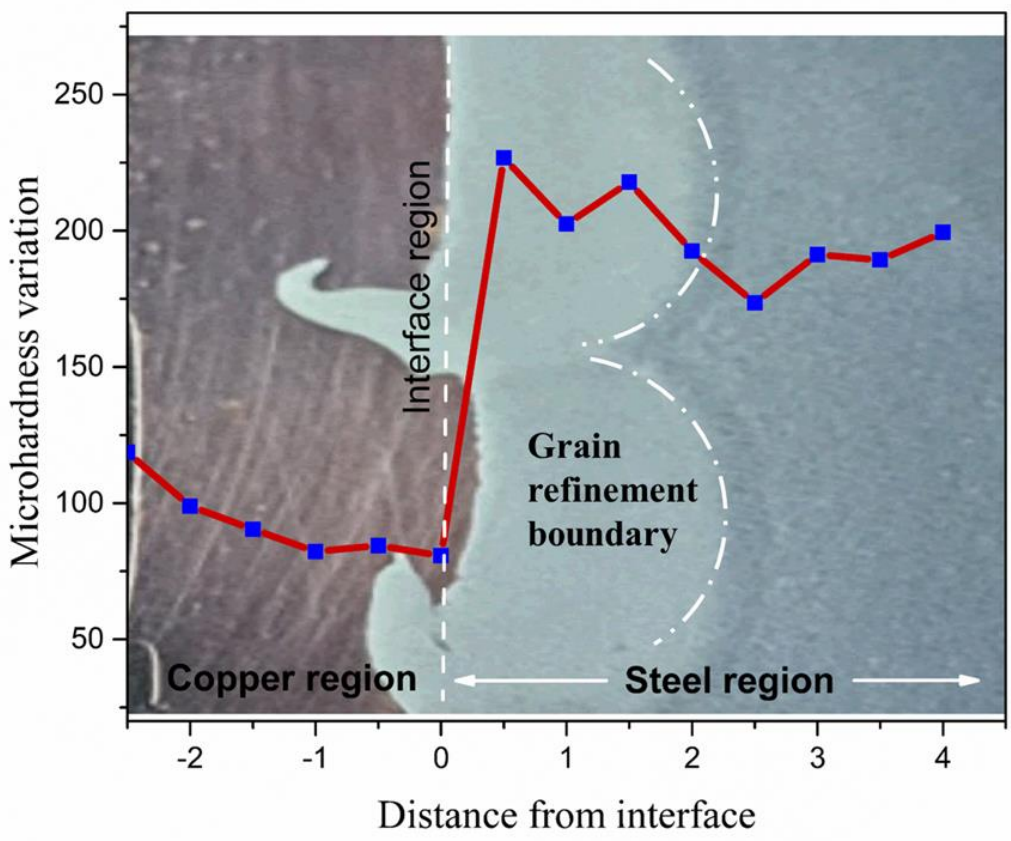

Figure 4-38 Microhardness variation across the interface from copper to steel

Figure 4-39 shows the variation of average microhardness across the base copper, clad copper top, and copper top region after 1.5 mm removal. No abrupt change in microhardness variation was recorded. The results demonstrate that clad copper regions show a minor improvement in microhardness with respect to base copper, which can be attributed to multipass stirring action on the copper surface. During the

cladding operation, the stirring action of tool travel results in the piercing and redistribution of copper regions.

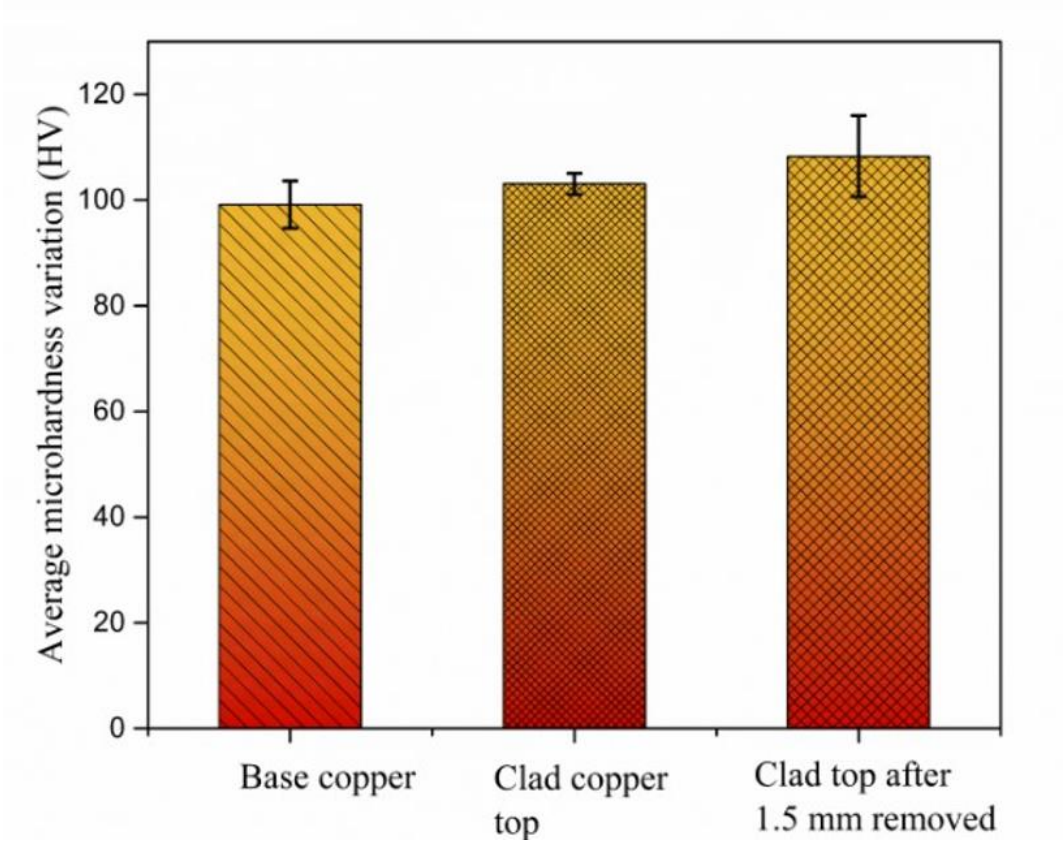

Figure 4-39 Average microhardness variation across copper top surface

4.13 XRD analysis of cladded samples

XRD analysis was carried out on the as-received copper, steel, clad copper top, and transverse cross section of the clad. A comparative analysis was performed on the top surface of cladded samples to determine if mild steel substrate material has reached the top surface of clad material. The flow of material during FSW can cause the substrate material to flow up to the top surface. In such an event, the surface properties of the clad layer can deteriorate. The XRD analysis of the transverse cross section was also carried out to trace out the possibility of intermetallic formation, which may have taken place near the interface region.

The matching of peaks was done by X'Pert High Score Plus software. Figure 4-40a refers to the XRD peak of as-received copper, where major diffraction peaks were observed at 43.41°, 50.48°, 74.15°, and 89.90° and were matching with ICSD file number 98-005-3755. Figure 4-40b shows the XRD peak of mild steel, where major diffraction peaks were observed at 44.61°, 82.28°, and 64.92° and were matching with ICSD file number 98-063-1729. Comparative XRD peaks from base copper, the top surface of a single-pass cladded copper top, and a multi-pass cladded copper top have been shown in Figure 4-40c and it is evident that no new distinguishing peaks were visible, clearly suggesting that all the peaks are of copper and mild steel substrate material could not reach the top nor that intermetallic formation took place at the top surface. Consequently, it can be claimed that no dilution of clad material was present on the top surface of the cladded layer.

The results of the XRD analysis carried out on the transverse cross section are shown in Figure 4-40d. New phases corresponding to intermetallics have been detected, and peaks corresponding to $Cu_{0.8}Fe_{0.2}$ were found to be matching with ICSD file number 98-010-2894 and peaks corresponding to $Cu_{0.3}Fe_{1.7}$ matched with ICSD file number 98-062-7297, indicating the formation of the above mentioned intermetallics on the transverse cross section of the cladding. Intermetallic formation is not desirable, and from the obtained peaks, it is confirmed that they are present only at the interface, buried deep inside. Also, their amount is comparatively small. There is no considerable drop in mechanical properties, although there is a slight dip in ductility, which can be attributed to the small amount of intermetallic formed.

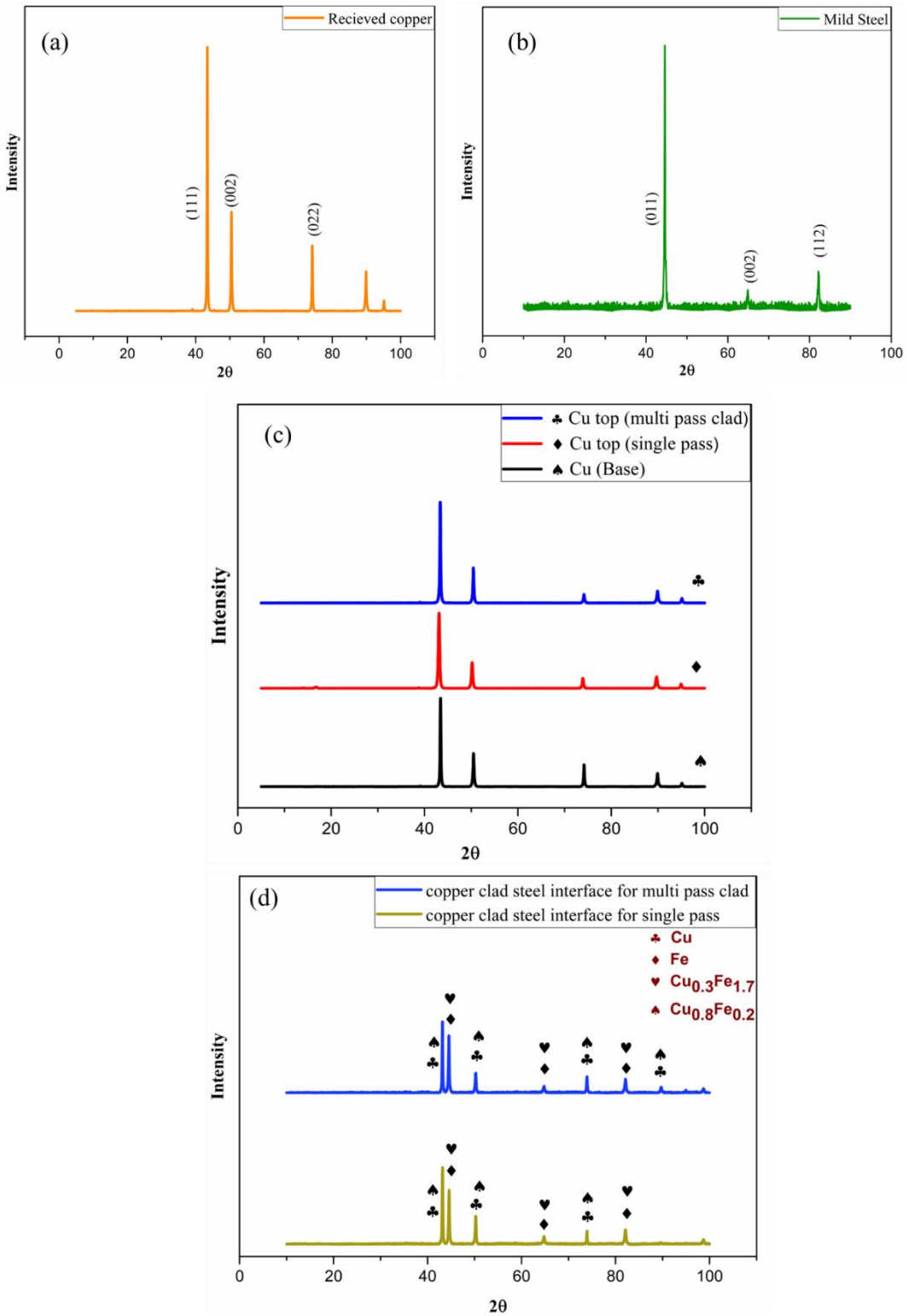

Figure 4-40 XRD peaks of (a) base copper (b) mild steel substrate (c) top surface of copper clad after single pass and triple pass clad top compared with XRD of base copper (d) transverse cross section indicating presence of intermetallics

4.14 Corrosion results

Potentiodynamic test scans were conducted in a 3.5 NaCl solution in a three-electrode cell on an Autolab 302N. Base copper or copper cladded sample served as the working electrode, with a test area of 1 cm^2. The reference electrode was a saturated calomel electrode, and the counter electrode was a platinum mesh with a surface area significantly larger than that of the working electrode. Before performing the corrosion tests, E_{ocp} was analysed to ensure a steady potential over time. Therefore, PDS tests were done after 30 minutes of E_{ocp} measurements. Tests were performed at a scan rate of 2.45 mV/s, and a potential range of (-1.27 V to +1.0 V) was used.

Copper in a neutral chloride solution forms the initial corrosion product as cuprous chloride (CuCl). This cuprous chloride is slightly unstable in dilute sodium chloride and reacts further to produce cuprous oxide (cuprite), which is the main constituent of thick scales. This cuprous oxide is generally oxidised over time to form cupric hydroxide ($Cu(OH)_2$) [216, 217], and the same has been shown illustratively in Figure 4-41.

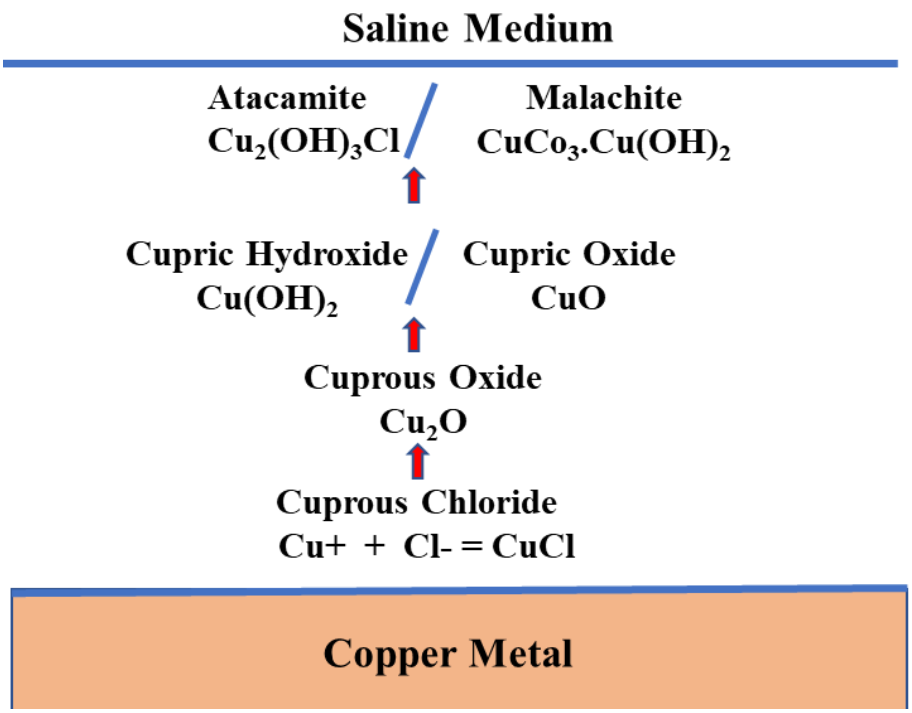

Figure 4-41 Stages of copper corrosion in chloride solution

Prior to performing the corrosion experiments, open circuit potential was collected to get a stable potential over time. After 30 minutes of E_{ocp} readings, PDS measurements were made. The time dependences of E_{ocp} for base copper, FSWed clad copper top, and clad top obtained after 1.5 mm removal are presented in Figure 4-42. It can be observed that the E_{ocp} values of base copper were higher than those of clad copper for both conditions. E_{ocp} values for base copper remained stable at around -215 mV, while the E_{ocp} values for clad conditions were more negative. E_{ocp} represents corrosion susceptibility, and the shifting of Eocp up, i.e., on the more positive side, indicates more corrosion resistance [218].

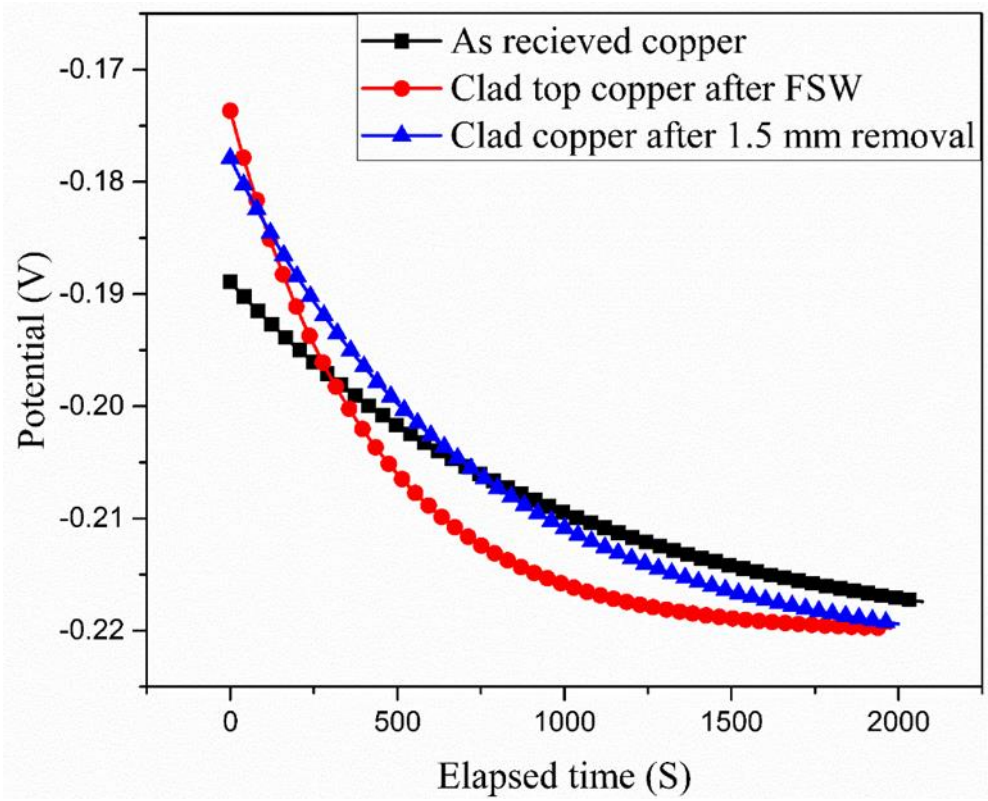

Figure 4-42 Open circuit potential variation for base copper, clad copper top, and clad top after 1.5 mm removal

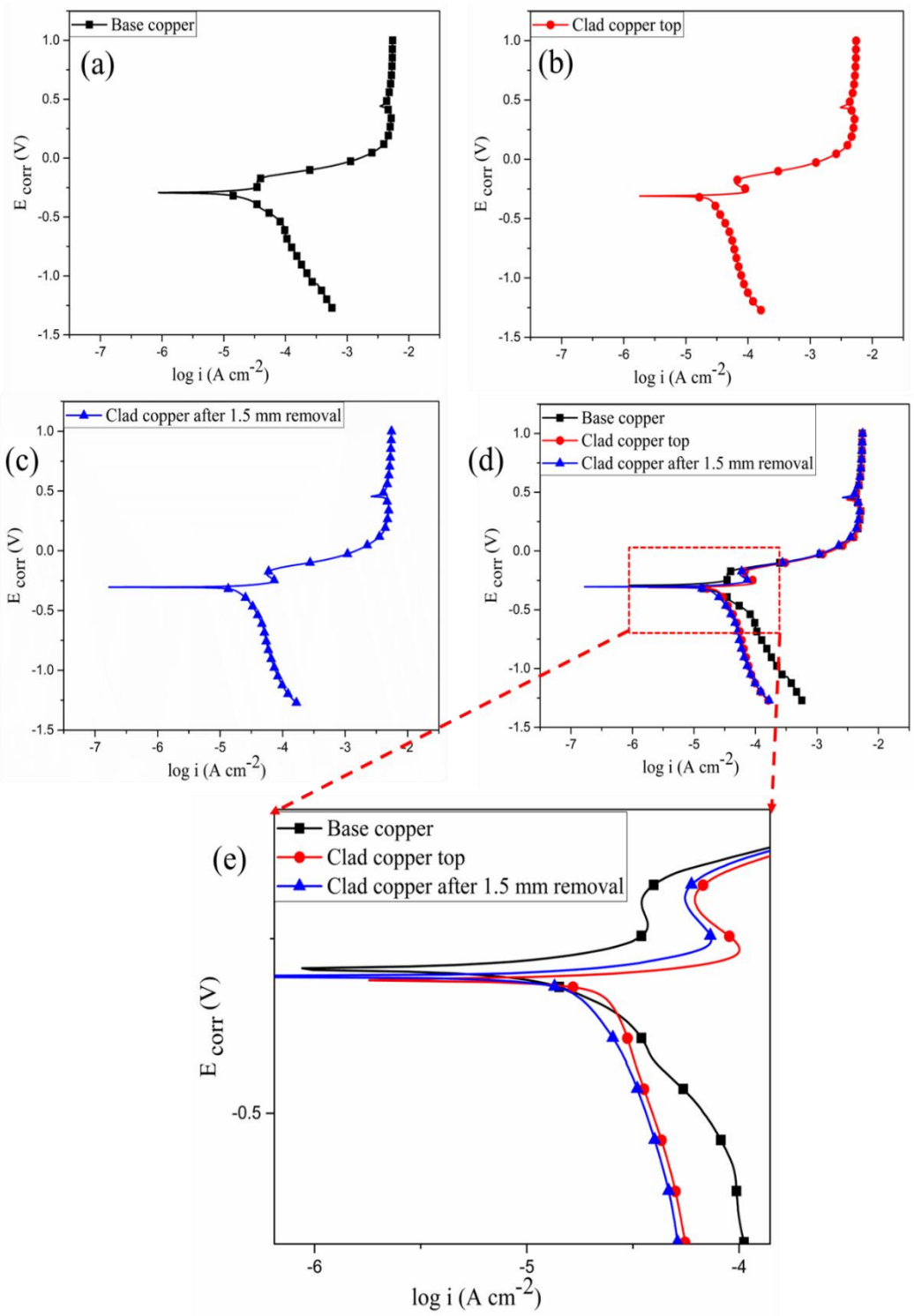

Figure 4-43 Tafel plots for (a) base copper (b) clad top copper (c) clad top copper after 1.5 mm removal (d) superimposed tafel plots (e) enlarged view of the same

The corrosion rate for base copper and cladded copper was determined using tafel analysis. An estimation was tried to be established for copper corrosion behaviour due to the multipass friction stir cladding technique, i.e., whether corrosion properties improved or degraded with FSW passes. The anodic and cathodic polarization curves for the corroded base and cladded copper are shown in Figure 4-43. Figure 4-43a is for base copper, while Figure 4-43b is for the top surface of the cladded samples, and Figure 4-43c represents the polarization curves for the clad top after the removal of the top 1.5 mm thickness. Figure 4-43d shows the results of all the tafel graphs superimposed in a single plot. A magnified view of the same has been shown in Figure 4-43e, where PDS scan results can be seen more explicitly. Tafel extrapolation of the cathodic or anodic polarisation curve can be used to calculate the corrosion rate using equation (2) [219].

$$\text{Corrosion rate (mm/yr)} = 3.27 \times 10^{-3} \times I_{corr} \times (\text{EW/density}) \quad \ldots\ldots\text{eq (2)}$$

where I_{corr} is the corrosion current density in $\mu A/cm^2$, EW is the equivalent weight of copper (taken as 31.8 g), and the density of the copper as 8.96 g/cm^3.

Table 4 Corrosion parameters

Condition	Ecorr (mV)	Icorr (μ/A/cm$^{2)}$	Corrosion rate (mm/yr)
Base copper	-294.2	20.16	0.23
FSWed clad copper top	-309.6	25.3	0.29
FSWed clad top after 1.5 mm removal	-304.83	22.33	0.26

From the polarisation curve in Figure 4-43 and the data in Table 4, it was observed that nearly all the samples exhibited similar corrosion behaviour. On further investigation,

it was observed that E_{corr} values were slightly more positive for the base copper in comparison to E_{corr} values for clad conditions. The corrosion rate for base copper, i.e., 0.23 mm/yr, was the lowest, and the corrosion rate for copper top clad was 0.29 mm/yr, while the corrosion rate for the clad top after 1.5 mm removal was 0.26 mm/yr. Obtained results suggest that no severe degradation has taken place in copper due to multipass cladding, and its capability in protecting the steel substrate is fulfilled.

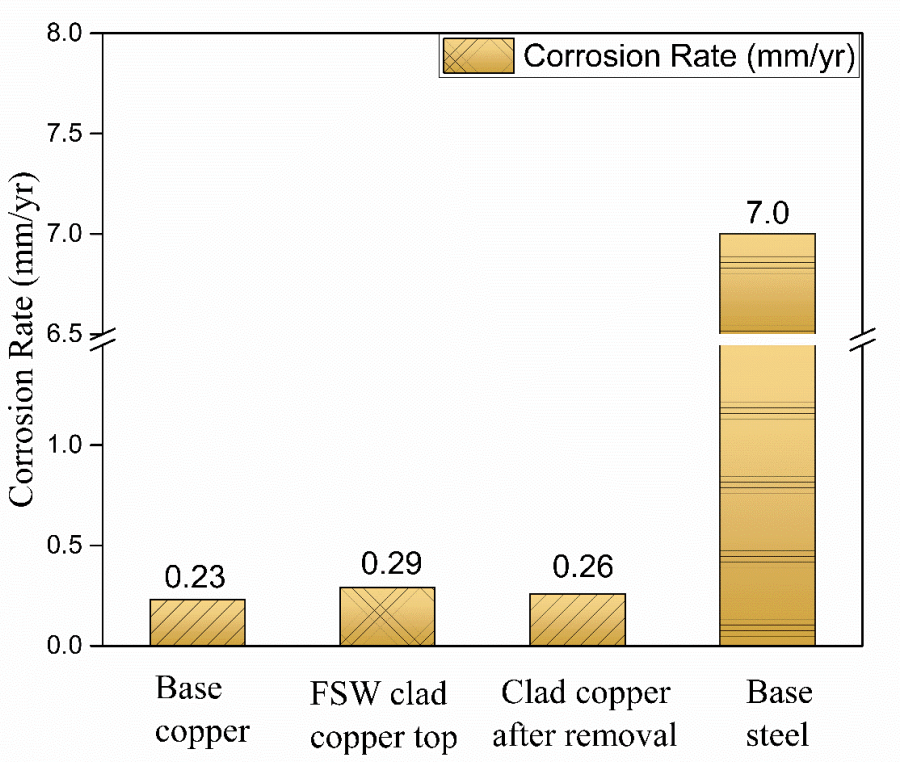

Figure 4-44 Comparison of corrosion rate of base copper, clad copper top, clad copper top after removal, vs corrosion of mild steel (taken from reference)[192]

Figure 4-44 compares the corrosion rate of base copper, clad copper top, and clad top after 1.5 mm removal, with respect to the corrosion rate of mild steel reported in the literature [192]. It can be concluded that a layer of copper on steel prevents the substrate from severe degradation, as copper clad showed a significantly lower

corrosion rate of nearly 0.29 mm/yr in comparison to the reported corrosion rate of 7 mm/yr for mild steel.

It was also observed that the corrosion rate of copper in cladded conditions (clad top and clad top after removal) was nearly the same and comparable to that of base copper. The increase in corrosion rate for clad conditions is only slightly higher than the corrosion rate of base copper. The difference is not significant enough to conclusively prove that FSW clad plate has poor corrosion properties.

4.14.1 SEM of corroded samples

Figure 4-45 compares the SEM of the corroded sample for the base copper and copper cladded mild steel on the clad top and the top surface obtained after 1.5 mm of removal of the copper top layer. Figure 4-45a shows the SEM micrograph of the sample taken at the boundary of the corroded and uncorroded regions. The transition boundary layer, with the uncorroded base region on the left and the region on the right, depicts the onset of corrosion. Figure 4-45(b, c) shows the SEM surface morphologies of the base copper sample after the potentiodynamic polarisation test for the as received condition at low and high magnifications. The corrosion attack is clearly visible in the micrographs, and the corrosion effect seems to be smooth for the base copper. Figure 4-45(d, e) shows the SEM images for the cladded copper top region after corrosion. A slightly higher corrosion attack was found for the clad top portion with respect to the base copper, which agrees with the potentiodynamic test results. Additionally, the appearance of CuO has been observed covering the surface, whose peaks have been detected in the XRD analysis. Figure 4-45(f, g) shows the corroded images of the clad top copper after 1.5 mm of removal from the top. Corrosion micrographs show groove paths, and the corrosion observed for this condition reveals less corrosion compared

to the clad top condition. Thus, it can be stated based on SEM observation of corroded samples that oxide formation was observed for the clad copper top, while groove path formation was observed for the clad top portion after removal, while smooth corrosion was observed for the base copper, which agrees with the potentiodynamic results.

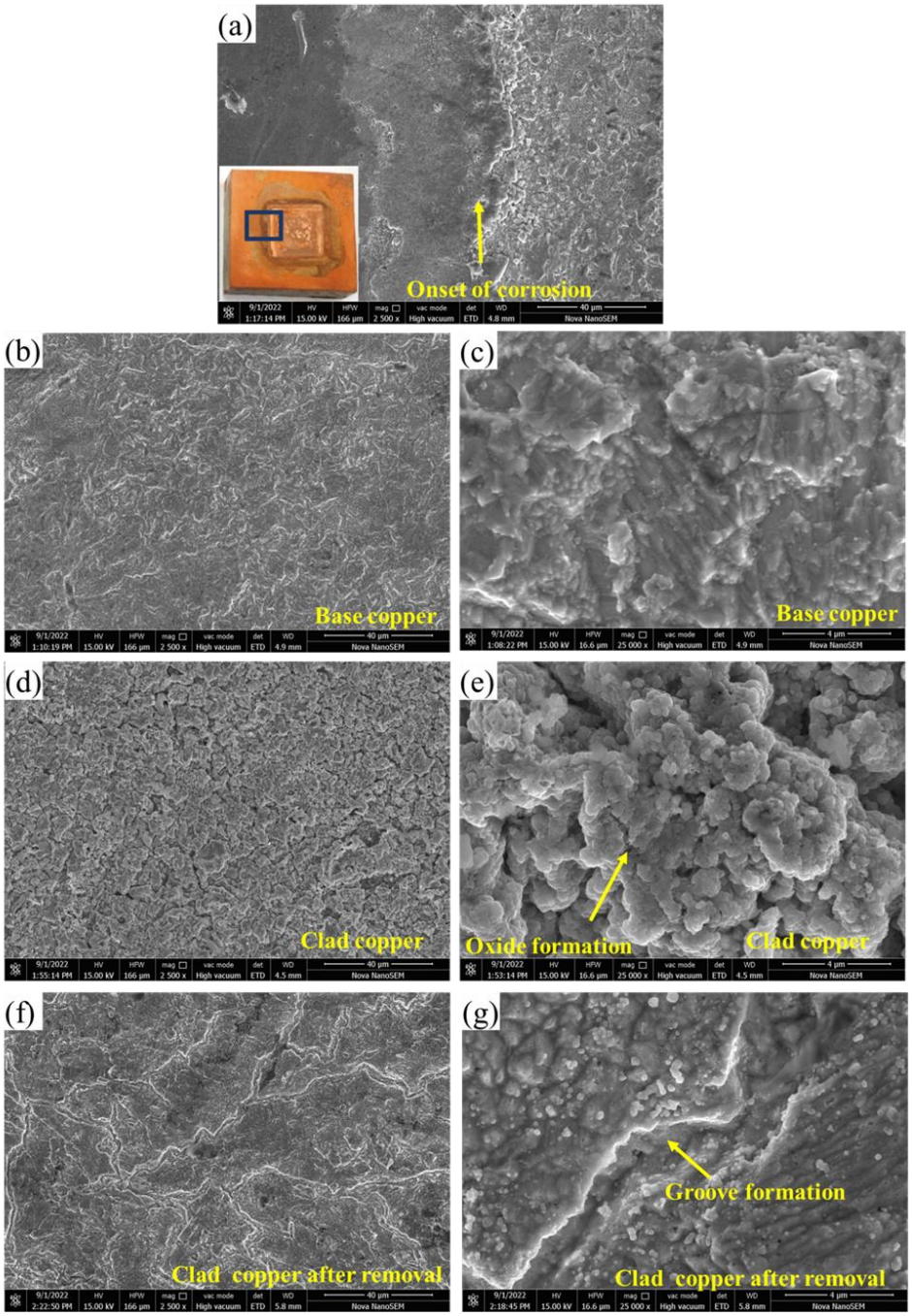

Figure 4-45 SEM images post corrosion (a) showing onset of corrosion boundary (b, c) base copper at low and high magnifications depicting smooth corrosion features (d, e) clad copper top depicting oxide formation (f, g) clad copper after 1.5 mm removal demonstrating groove path formation

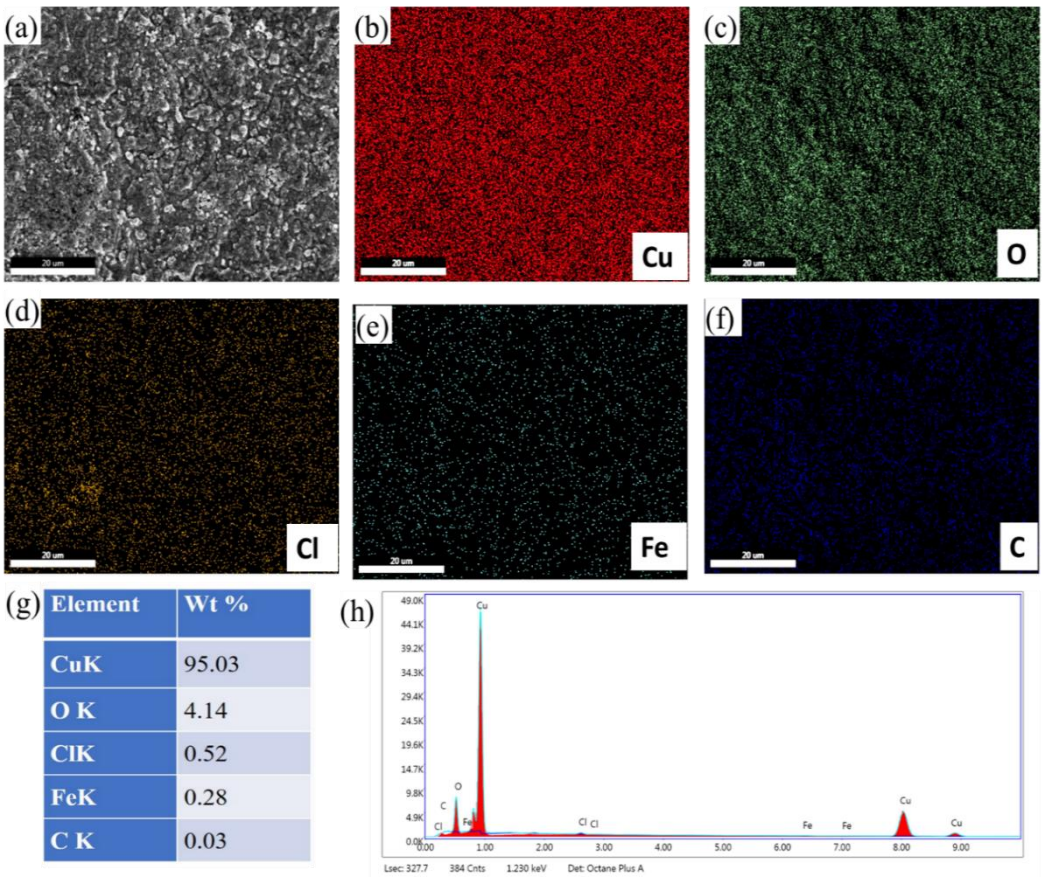

Element	Wt %
CuK	95.03
O K	4.14
ClK	0.52
FeK	0.28
C K	0.03

Figure 4-46 Demonstrating (a) SEM Image of corroded clad top copper (b) EDS map demonstrating copper (c) oxygen in the corroded region (d) chlorine (e) iron (f) carbon (g) EDS quantification (h) peak spectra for same

Figure 4-46 shows the EDS map images of the corroded, clad top copper region. The SEM image of the corroded region is shown in Figure 4-46a. The EDS maps of copper, oxygen, chlorine, iron, and carbon are shown in adjacent images. The elemental composition of the corroded region has been shown in Figure 4-46g, showing the presence of oxygen due to oxide phases. The elemental spectra of the same region have been shown in Figure 4-46h, showing major peaks of copper and oxygen.

4.14.2 XRD analysis of corroded samples

Figure 4-47 shows the XRD patterns of the friction stir cladded copper surfaces in comparison with the received copper after the corrosion test. The results showed that the as-received copper exhibited four peaks observed at 2θ values of 43°, 50°, 74°, and 89°, indicating the characteristic peaks of Cu metal and matching ICSD file number 98-005-3755. The peaks of corroded samples of the base, cladded copper top, and 1.5 mm removed clad layer exhibited similar peaks with the presence of ZnO (ICSD 98-016-6360) and Cu_3Zn (ICSD 98-062-9461).

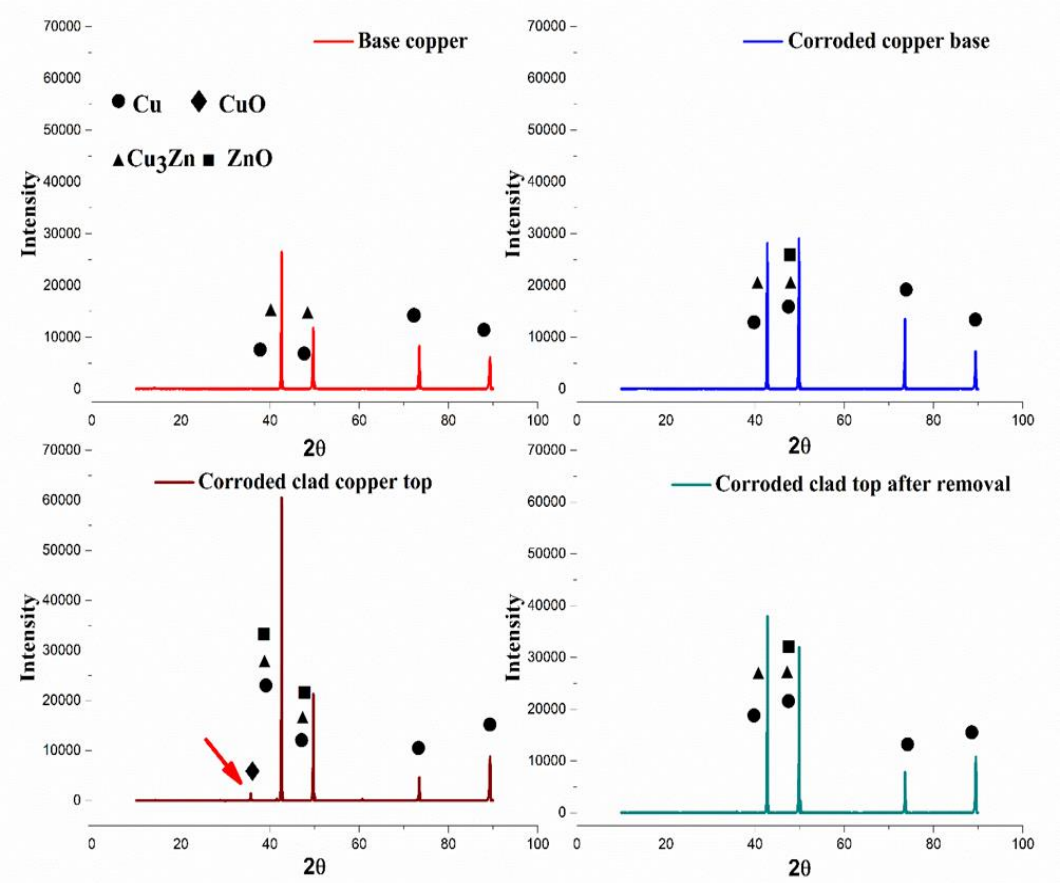

Figure 4-47 XRD peaks for (a) base copper (b) corroded base (c) corroded clad top copper (d) corroded clad top copper after removal

A visible demonstration of enhanced intensity of peaks is observed for the copper top clad region, indicating surface modification and the appearance of an extra phase due

to friction stir cladding. The clad top copper region demonstrated an extra peak of low intensity at 38°, confirming the presence of CuO (ICSD 98-004-3181). This agrees with the potentiodynamic results and SEM images confirming the presence of an oxide layer on the clad top copper, resulting in the observation of extra peaks. In all the other remaining cases, no extra peak presence was observed.

4.14.3 AFM 2D and 3D analysis

AFM has proven to be a powerful tool to distinguish surface appearance at the nano- to microscale level and has become a superior choice in the area of corrosion analysis. The two-dimensional (2D) and three-dimensional (3D) AFM images and corresponding height profiles of base copper, along with the corroded clad samples due to the attack of saline solution, are presented in this section.

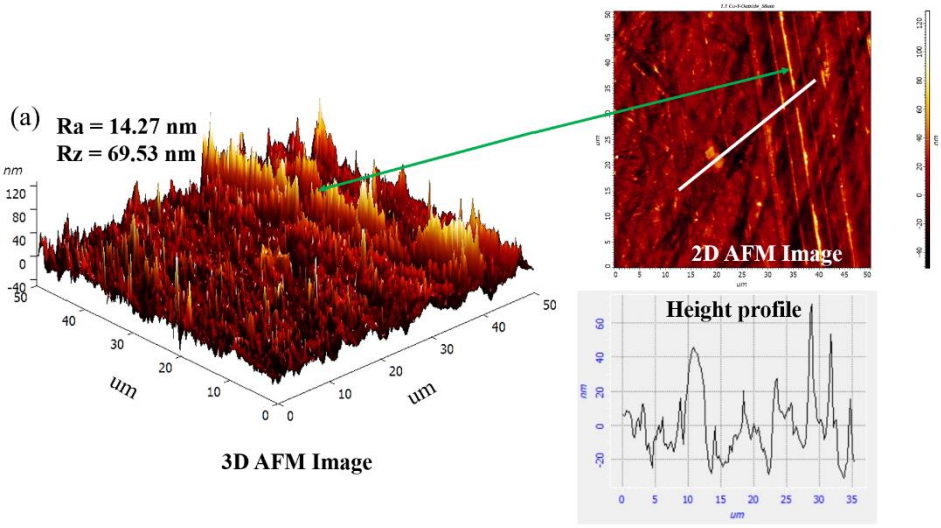

Figure 4-48 3D and 2D AFM images along with height profile for base copper

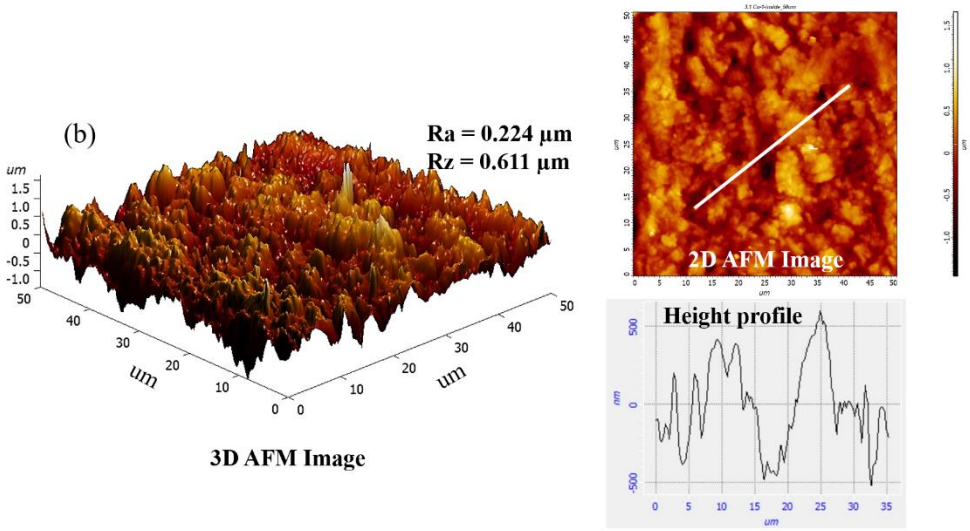

Figure 4-49 3D and 2D AFM images along with height profile for corroded base copper

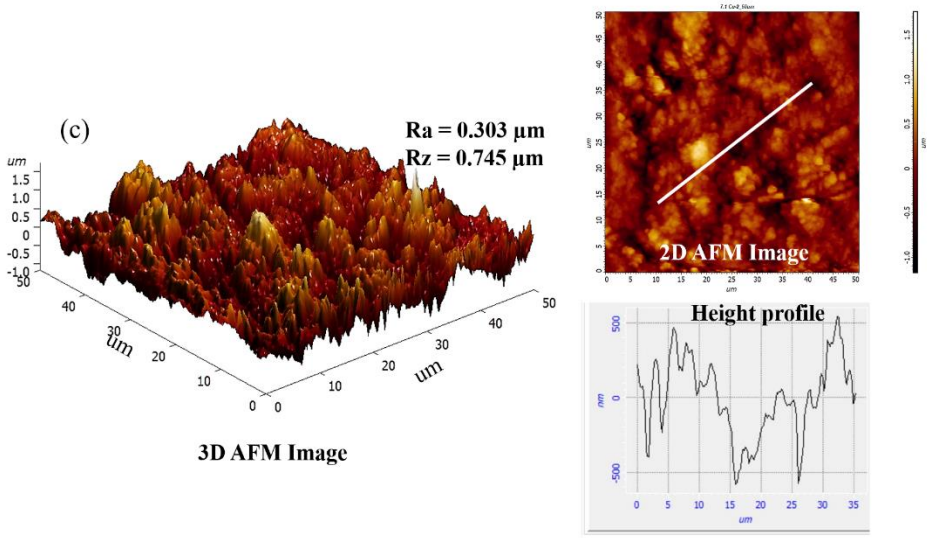

Figure 4-50 3D and 2D AFM images along with height profile for corroded clad top

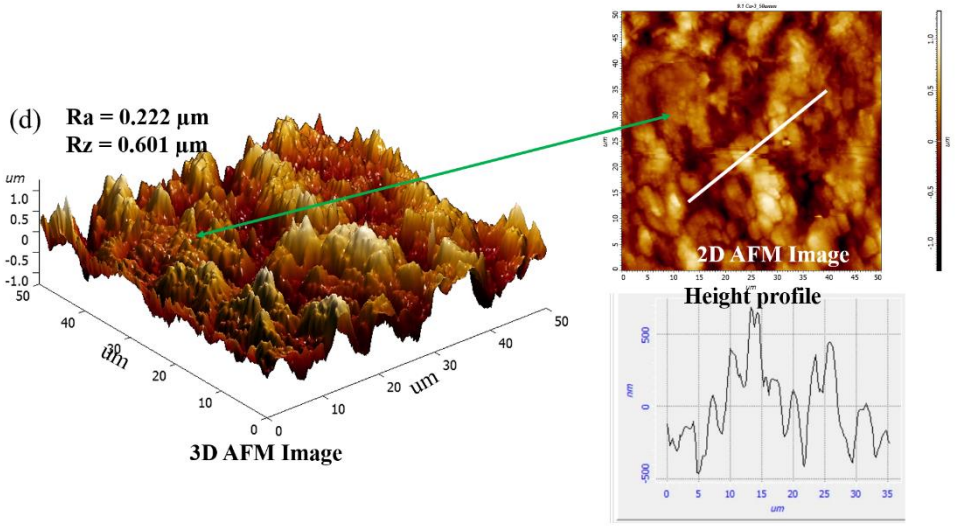

Figure 4-51 3D and 2D AFM images along with height profile for corroded copper top after removal

Figure 4-48 shows the AFM images of the base copper obtained before the potentiodynamic polarisation test. The AFM 2D and 3D images depict the surface topography typical of a mechanically processed surface. The sample highlights a uniform surface before undergoing corrosion study, having an average roughness (Ra) of 14.27 nm and a ten-point mean roughness (Rz) of 69.53 nm, which is also supported by the height profile, which represents average surface peaks of 20 nm and the highest peak touching 60 nm.

The AFM images of the corroded base are shown in Figure 4-49 which depicts the changed surface appearance compared to before corrosion. Pits arising out of corrosion can be seen all over the surface, which suffered damage as a result of the corrosive attack of the saline solution. The corroded base sample shows (Ra = 0.224 µm and Rz = 0.611 µm), confirming higher roughness in comparison to base copper. It consisted

of a surface with smaller pits, which clearly signifies that the corrosion rate of base copper was considerably low. The phenomenon can be further evidenced by the height profile, which demonstrates that the depth of pits formed during corrosion reached up to 500 nm in depth compared to an uncorroded sample with peaks of 20 nm.

The AFM images of the clad copper top are shown in Figure 4-50. Features similar to corroded bases are observed over here. The rough structure comprises deep and slightly larger pits due to the aggressive attack of saline solution. The clad top copper shows the highest average roughness Ra of 0.303 μm and Rz of 0.745 μm. The 2D image in Figure 4-50 comprises darker spots suggesting deep grooves, supported by a height profile that suggests the lowest groove point crossing 500 nm, suggesting severe corrosion for this condition, which also validates the potentiodynamic test results. Figure 4-51 shows the AFM results for the corroded clad copper region after 1.5 mm removal and suggests similar results as clad top results with the lesser intensity of height profile peaks, i.e., below 500 nm and an average roughness Ra of 0.222 μm. Based on the AFM results, it can be concluded that the highest corroded surface was observed for the clad top with deep pits, agreeing with the potentiodynamic test results.